Annu. Rev. Earth Planet. Sci. 1995. 23:337–74

RADAR INVESTIGATION OF MARS, MERCURY, AND TITAN

Duane O. Muhleman

Division of Geological and Planetary Sciences, 170-25, California Institute of Technology, Pasadena, California 91125

Arie W. Grossman

Laboratory for Millimeter-Wave Astronomy, Department of Astronomy, University of Maryland, College Park, Maryland 20742

Bryan J. Butler[1]

Division of Geological and Planetary Sciences, 170-25, California Institute of Technology, Pasadena, California 91125

KEY WORDS: coherent backscatter, multiple scattering, stealth

INTRODUCTION

Radar astronomy is the study of the surfaces and near surfaces of Solar System objects using active transmission of modulated radio waves and the detection of the reflected energy. The scientific goals of such experiments are surprisingly broad and include the study of surface slopes, fault lines, craters, mountain ranges, and other morphological structures. Electrical reflectivities contain information about surface densities and, to some extent, the chemical composition of the surface layers. Radar probes the subsurface layers to depths of the order of 10 wavelengths, providing geological mapping and determinations of the object's spin state. Radar also allows one to study an object's atmosphere and ionic layers as well as those of the interplanetary medium. Precise measurements of the time delay to surface elements provide topographic maps and powerful information on planetary motions and tests of gravitational theories such as general relativity. In this paper, we limit our discussion to surface and near-surface probing of Mercury, Mars, and Titan and review the

[1]Currently at the National Radio Astronomy Observatory, Socorro, New Mexico.

0084-6597/95/0515-0337$05.00

work of the past decade, which includes fundamentally new techniques for Earth-based imaging.

The most primitive experiments involve just the measurement of the total echo power from the object. The most sophisticated experiments would produce spatially resolved maps of the reflected power in all four Stokes' parameters. Historically, the first experiments produced echoes from the Moon during the period shortly after World War II (see e.g. Evans 1962), but the subject did not really develop until the early 1960s when the radio equipment was sufficiently sensitive to detect echoes from Venus and obtain the first Doppler strip "maps" of that planet. The first successful planetary radar systems were the Continuous Wave (CW) radar at the Goldstone facility of the Caltech's Jet Propulsion Laboratory and the pulse radar at the MIT Lincoln Laboratory. All of the terrestrial planets were successfully studied during the following decade, yielding the spin states of Venus and Mercury, a precise value of the astronomical unit, and a host of totally new discoveries concerning the surfaces of the terrestrial planets and the Moon. This work opened up at least a similar number of new questions. Although the early work was done at resolution scales on the order of the planetary radii, very rapid increases in system sensitivities improved the resolution to the order of 100 km, but always with map ambiguities. Recently, unambiguous resolution of 100 m over nearly the entire surface of Venus has been achieved from the *Magellan* spacecraft using a side-looking, synthetic aperture radar. Reviews of the work up to the *Magellan* era can be found in Evans (1962), Muhleman et al (1965), Evans & Hagfors (1968, see chapters written by G Pettengill, T Hagfors, and J Evans), and Ostro (1993). The radar study of Venus from the *Magellan* spacecraft was a tour de force and is well described in special issues of *Science* (volume 252, April 12, 1991) and in the *Journal of Geophysical Research* (volume 97, August 25 and October 25, 1992). Venus will not be considered in this paper even though important polarization work on that planet continues at Arecibo, Goldstone, and the Very Large Array (VLA).

In this paper we review the most recent work in Earth-based radar astronomy using new techniques of Earth rotation, super synthesis at the VLA in New Mexico (operated by the National Radio Astronomy Observatory), and the recently developed "long-code" techniques at the Arecibo Observatory in Puerto Rico (operated by Cornell University). [Note: It was recently brought to our attention that the VLA software "doubles" the flux density of their primary calibrators. Consequently, it is necessary to half the radar power and reflectivity numerical values in all of our published radar results from the VLA/Goldstone radar.] The symbiotic relationship in these new developments for recent advances in our understanding of Mercury and Mars is remarkable. VLA imaging provides for the first time, unambiguous images of an entire hemisphere of a planet and the long-code technique makes it possible to map Mars and Mercury

using the traditional range-gated Doppler strip mapping procedure [which was, apparently, developed theoretically at the Lincoln Laboratory by Paul Green, based on a citation in Evans (1962)]. Richard Goldstein was the first to obtain range-gated planetary maps of Venus as reported in Carpenter & Goldstein (1963). Such a system was developed earlier for the Moon as reported by Pettengill (1960) and Pettengill & Henry (1962)). We first discuss the VLA synthesis mapping technique.

The use of the VLA as the radar receiving instrument allows one to make a spatial map of the echo power with a resolution only limited by the resolving power of the VLA. The ultimate resolution at the radar wavelength of 3.5 cm is 0.2 arc sec, achieved when the VLA is in its largest configuration with a maximum spacing between antenna elements of 36 km. This resolution corresponds to 145 km at a distance of 1 astronomical unit (AU). These values are actually the minimum fringe spacing for the instrument (at 3.5 cm), and the image resolution achieved in real maps is degraded by about 50%. These new techniques allowed observers at the VLA to obtain complete, unambiguous radar maps of the Earth-facing hemispheres of the terrestrial planets. The VLA/Goldstone radar has a bistatic configuration with the NASA/JPL 70-m antenna at Goldstone transmitting at a wavelength of 3.5 cm and with radiated power up to 460,000 watts in the monochromatic or CW mode. The exact transmitter frequency is tuned with a programmed local oscillator, which removes the Doppler shift caused by the the motion of the center of mass of the target planet with respect to the transmitter and the receiver system at the VLA. Thus, the reflected radar energy is received with the VLA 27-antenna interferometer as though the reflected flux density was "emitted" from a celestial, narrow-band spectral line source. The CW transmitted signal is Doppler-spread at reflection due to the relative rotational motion of each reflecting point on the planet. In principle, it is possible to take advantage of the Doppler strip resolution in the VLA mapping to greatly increase the spatial resolution in "one dimension." However, the available minimum frequency resolution at the VLA is insufficient to resolve in frequency planetary objects other than Mars and Saturn's rings. The maximum spectral width for the targets of interest are about 200, 400, 1340, and 28,000 Hz for Venus, Mercury, Titan, and Mars, respectively. Unfortunately, the *minimum* frequency resolution at the VLA is 381 Hz if just a single polarization is to be recorded; that value must be doubled if two polarized signals are to be recorded. The VLA/Goldstone radar utilizes a circularly polarized transmitted signal [usually Right Circular Polarization (RCP)] and it is desirable to receive the echo energy in both RCP and Left Circular Polarization (LCP), which dictates a minimum frequency resolution of 763 Hz. Thus, in the cases of Venus and Mercury, all of the echo energy is in a single spectral channel that is wider than the signal spectrum, causing a loss in sensitivity. If all four Stokes' parameters were to be measured,

another doubling of the minimum bandwidth to 1526 Hz would be required. Only then could the response in both the circular and two linear modes of polarization be derived from the amplitudes and phases measured in circular polarization.

The study of the physical properties of a planetary surface is greatly aided by measuring the polarization properties in the echoes. Quite generally, the strongest reflections from a natural surface will be obtained for circularly polarized transmitted signals by measuring the echo in the circular polarization opposite to that transmitted. This is because the polarization is reversed for a normal incidence, backscatter reflection from a smooth, infinite dielectric surface (see, e.g. Stratton 1941). The received signal in the opposite circular polarization has been called the "polarized," or "opposite sense circular" (OC), or simply the "opposite sense" (OS) signal. The received signal in the same circular polarization as transmitted has been called "depolarized," SC, or simply SS. We use the OS and SS notation in this paper without danger of confusion since linearly polarized experiments are not relevant for this review. The details of the physics of the reflection processes from natural surfaces is very complex and poorly understood. However, one can adopt the first-order view that the OS reflection is dominated by the incoherent sum of temporally brief coherent reflections from a changing ensemble of nearly flat regions, instantaneously aligned within a small solid angle along the backscatter direction. Actually, the incident polarized electric field drives currents in the surface layers, which are affected by the 3-dimensional polarizibilty of the material, creating a complex reflected electromagnetic wave. Empirical results over real terrain suggest that the OS echo is dominated by these pseudo-coherent reflections from local, flat mirror-like structures larger than the wavelength. Thus, the OS echo is dominated by the local surface slopes and the electrical reflectivity of these facets. A small fraction of the OS power is multiply scattered (and diffracted) on the surface and from within the near-surface layers into a more diffuse component. These fractions apparently depend on the absorption coefficient of the near-surface materials. In this first-order view of the reflection physics, the depolarized or SS echo arises from multiple reflections on the surface and multiple scattering within the near-surface materials, again dependent on the material's complex dielectric constant and texture. The empirical evidence shows that the depolarized echo is similar to the diffuse part of the OS echo but somewhat weaker for surfaces composed of the usual geological materials such as silicates and basalts. The situation is very different for planetary surface deposits that are poorly absorbing at the given wavelength; these are essentially transparent.

Goldstein & Morris (1975) made the first radar measurement of a Galilean satellite—Ganymede—but only in OS polarization. A systematic program on all four satellites was carried out at Arecibo by Campbell et al (1978).

They discovered that SS echoes were stronger than the OS echoes for the three icy satellites—Europa, Ganymede, and Callisto. We believe that the key to understanding this anomaly can be found in Goldstein & Green (1980), who considered the scattering of photons in a fractured, transparent medium. The scattering events are dominated by forward scattering at the interfaces, near the critical refraction angle. Consequently, the strong forward scattering tends to preserve the polarization, and the energy is strongly channeled back to the radar receiver without the polarization flip. Their calculations using the index of refraction for water ice are in good agreement with the measured ratios of the SS power to the OS power. A review of the observational work and some of the many theoretical ideas can be found in Ostro (1982). The strength of the polarization anomaly seems to decrease in going from Europa to Ganymede to Callisto, as does the visual albedo. This result suggests to us that the albedo variation is a manifestation of the dust/ice fractions in the satellites and an associated decrease in the medium's transparency from Europa to Callisto. More recently, Hapke (1990) and Hapke & Blewitt (1991) made significant advances in our understanding of the these phenomena. Hapke (1990) suggested that the strong backscatter measured from the icy Galilean satellites is caused by "coherent backscatter" in the medium. He postulated that the multiply scattered path of a "photon" through the essentially transparent medium is also followed by a photon in the reverse direction and that the emerging photons will be coherent and will combine in phase to form the reflected waveform. The coherent summing of the wave energy is much stronger than the incoherent sum of powers present in diffuse scattering off the surface. Perhaps more importantly, Hapke & Blewitt (1991) presented laboratory measurements of laser reflections from suspended silicate beads: These not only showed the strong peak power very near the backscatter direction but also displayed an anomalous SS/OS polarization ratio of about 1.5 (near the backscatter direction).

Even though we are far from understanding the detailed physics of the polarization properties in multiple scattering, the empirical evidence is sufficiently strong to use the above ideas in the interpretation of radar scattering from rough surfaces and partially transparent surfaces that display multiple scattering. In particular, we have a strong indicator of the presence of ice on a surface and a start toward the quantitative interpretations of the measurements from the polar regions of Mercury and Mars and from the entire surface of Titan. This topic forms a central thrust of this paper in parallel with the discussion of newly discovered radar features on the planets, including Stealth on Mars and the so-called radar basins on Mercury. In the next sections we review the most recent results on these three bodies from the viewpoint of planetary physics and geology.

MARS

Mars was first observed with radar in 1963 by Goldstein & Gilmore (1963). A recent review can be found in Simpson et al (1992). The planet is severely radar-overspread because of the rapid rotational rate and the full disk cannot be mapped with the standard range-gated Doppler spectrum technique. The time for the range modulation on the illuminating waveform to fully envelop Mars and return to the front edge of the planet is twice the radius divided by the speed of light. That value is the length of the modulation code that can be used without aliasing. Additional details on this limitation can be found in Green (1968) and in Hagfors & Kofman (1991). Consequently, until recently only the echo power around the front cap of Mars centered on the subearth point could be mapped. Nevertheless, the results from such work, while limited to the path of the subearth track at any opposition, have told us much about the Martian surface [see, for example, Harmon & Ostro (1985), Thompson et al (1992), and the review of Simpson et al (1992)]. However, the polar regions could not be studied, and much of the region on the equator was missed because of the geometrical circumstances of the oppositions since the 1960s.

None of these limitations were operative when the first Mars VLA/Goldstone radar experiments were performed in 1988; these yielded unambiguous maps of the entire observable hemispheres in two orthogonal modes of circular polarization. This work was reported in Muhleman et al (1991), hereafter called Paper I and in the thesis of Butler (1994), hereafter called Paper II (see also Butler et al (1993)). The 27 antennas of the VLA operate as $N(N-1)/2 = 351$ (for $N = 27$) simultaneous interferometers, which discreetly sample the Fourier spatial components of the observed radio source. The antennas are in a "Y" configuration with a maximum separation of 36 km between the end members of the Y for the experiments considered here. The 2-dimensional Fourier transform of the set of flux-density amplitudes and phases measured in each antenna pair yields a 2-dimensional, unambiguous spatial map of the source convolved with the effective beam of the array. [See Thompson et al (1991) for a thorough discussion of interferometric arrays.] As the source passes the observatory from the eastern to the western horizon, the projection of the individual antenna-pair baselines rotate on the source and effectively fill the array aperture (depending on source declination). However, because of the 24.62-h rotation of Mars, this rotational synthesis technique cannot be used in practice. Instead, Mars was observed in 12–15 minute snapshots, affording essentially zero baseline rotations. Because the exact positions of the antennas are known to a fraction of the 3.5-cm wavelength and the signal phases are accurately calibrated, the effective beam could be accurately deconvolved from the data, producing excellent images as shown in Figure 1. The calibration of the data used the standard technique of observing known point radio sources. Additional phase self-calibration was achieved by using the specular spike in the polarized radar

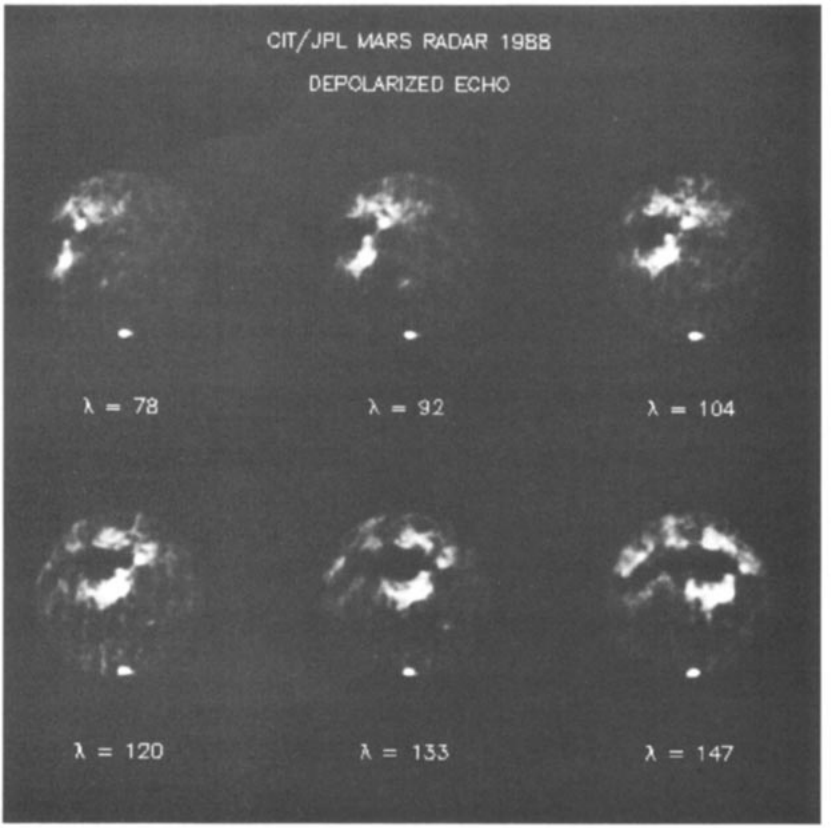

Figure 1 Radar images of Mars at 3.5 cm wavelength at about hourly intervals. The central meridian longitudes are indicated. The south pole is tilted toward Earth.

echo. Detailed results of these observations can be found in Papers I and II and in Butler (1994). Here, we review the highlights, concentrating on Stealth, the north and south polar regions, and images of the Tharsis and Elysium volcanic provinces. The Mars discussion concludes with a review of the radar results in the polar regions.

Stealth

Perhaps the most remarkable feature discovered by radar imaging of Mars is the huge region with effectively zero reflectivity dubbed "Stealth" in Paper I. Two outlines of the region are shown in Figure 2 superimposed on a gray-scale composite radar image of the entire region (Paper II). The dashed contour is the Stealth boundary published in Paper I, based on the 1988 observations. Stealth

was observed again in 1993 at near-normal incidence and the new contour based on all the data is indicated by the solid lines in Figure 2. It can be seen from the gray-scale image that very low reflectivity material continues westerly beyond the 170° meridian. The reflectivity limit for the 1988 data was 0.5% and that for the 1993 data was 0.25%. We define the "reflectivity" as the radar cross section per unit projected area. We computed it from the ratio of the reflected power in a given beam (in either polarization) to the total power that would be reflected from the unity reflector with the same cross-sectional area as the beam. Our reflectivities include both the electrical effects due to the surface material dielectric properties and the backscatter "gain" caused by surface roughness or multiple scattering effects. Stealth extends nearly 2500 km along the equator, with its east boundary at the base of the Tharsis volcanic ridge. Tentative explanations for this feature, which is unique among the terrestrial planets, are given in Papers I and II, along with estimates of its composition and minimum depths of the underdense layer.

From a pure physics standpoint, Stealth is a region with a nearly perfect impedance match to free space. Of course, there is true reflection from it that is below the sensitivity of these short-wavelength experiments. JK Harmon (private communication, 1994) has obtained new observations at a wavelength of 13 cm that display the stealth effect but none of the details are published

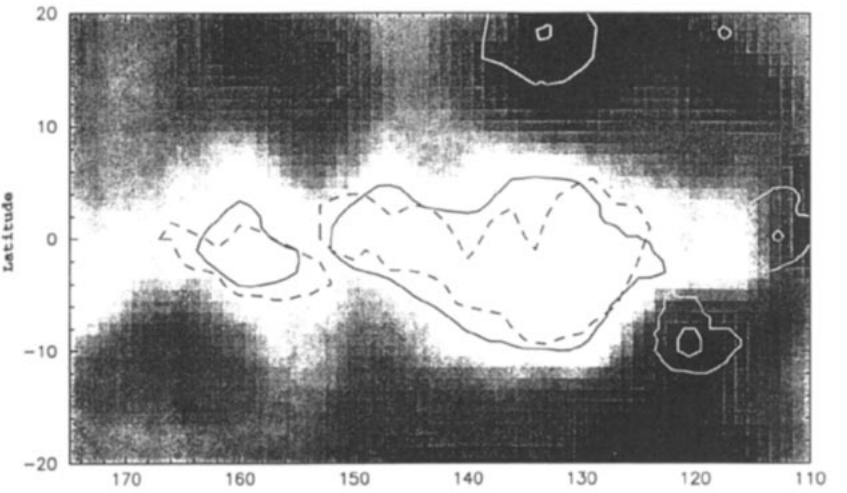

Figure 2 Radar image of the Stealth region on Mars shown in a cylindrical projection of the effective normal incidence SS reflectivity. The solid line shows the best estimate of Stealth from all 3.5-cm data; the dashed line is from Muhleman et al (1991). The Tharsis volcano calderea and shields are suggested by the while lines. (From Butler 1994.)

yet. RF Jurgens (private communication) has Goldstone observations of the stealth effect along the southern edge of the feature in 1992. It is clear that Stealth is made of material to some depth that both reflects very little centimeter wavelength energy and does not exhibit a significant reflection from its lower boundary, which must be higher density material typical of the rest of the Martian surface. Furthermore, the medium is free of rocks and clumps of centimeter sizes and larger that would act as volume scatterers. The absence of a sublayer reflection requires that the stealthy material has sufficient ohmic absorption properties to suppress the reflection from the lower boundary, i.e. the layer possesses some opacity. If the mean depth of the layer is D and the mean absorption coefficient per unit length is k_v, the optical depth is

$$\tau = k_v D. \tag{1}$$

Using the reasonable concept that the lower boundary is rough on the scale of the wavelength, or equivalently, that the true depths vary significantly over an area on the scale of the pixels (or on the scale of the first Fresnel zone), the effective reflectivity can be written

$$R = R_0 + \frac{R_1(1 - R_0)^2 e^{-2\tau}}{1 - R_0 R_1 e^{-2\tau}}, \tag{2}$$

where R_0 is the power reflectivity of the surface layer material and R_1 is the effective reflectivity of the lower boundary interface. If the surface layer is infinitely deep, the observed reflectivity is just R_0, which must be less than 0.0025 to match the upper limit from the observations. Since we have only observed an absence of a radar reflector at this limit, the concept of a surface gain has no meaning. Consequently, we tentatively interpret the limit of 0.0025 as that of the electrical reflectivity for a smooth surface at normal incidence. If the layer were perfectly transparent, i.e. $\tau = 0$, Equation (2) yields

$$R = R_0 + \frac{R_1(1 - R_0)^2}{(1 - R_0 R_1)} \sim R_1 + R_0,$$

where the approximation holds because R_0 is very small in any case. If Stealth were a homogeneous layer of infinite depth with a complex dielectric constant $E = E_r - i E_i$, then the reflectivity as a function of the real part of the dielectric constant would be that shown in Figure 3*a*. The three lines shown are for loss tangents, $\tan(d) = (E_i/E_r)$ equal to 0.005, 0.020, and 0.045, and demonstrate that the reflectivity of a homogeneous half-space is practically independent of the absorption properties of the medium. The observed upper limit of the Stealth reflectivity of 0.0025 shows that such a half-space must have a real dielectric constant less than about 1.25, i.e. it must be extremely underdense relative to known surfaces on the terrestrial planets. The reflectivity computed from Equation (2) with $R_0 = 0.0025$ and $R_1 = 0.10$ and 0.25 is shown in Figure 3*b*.

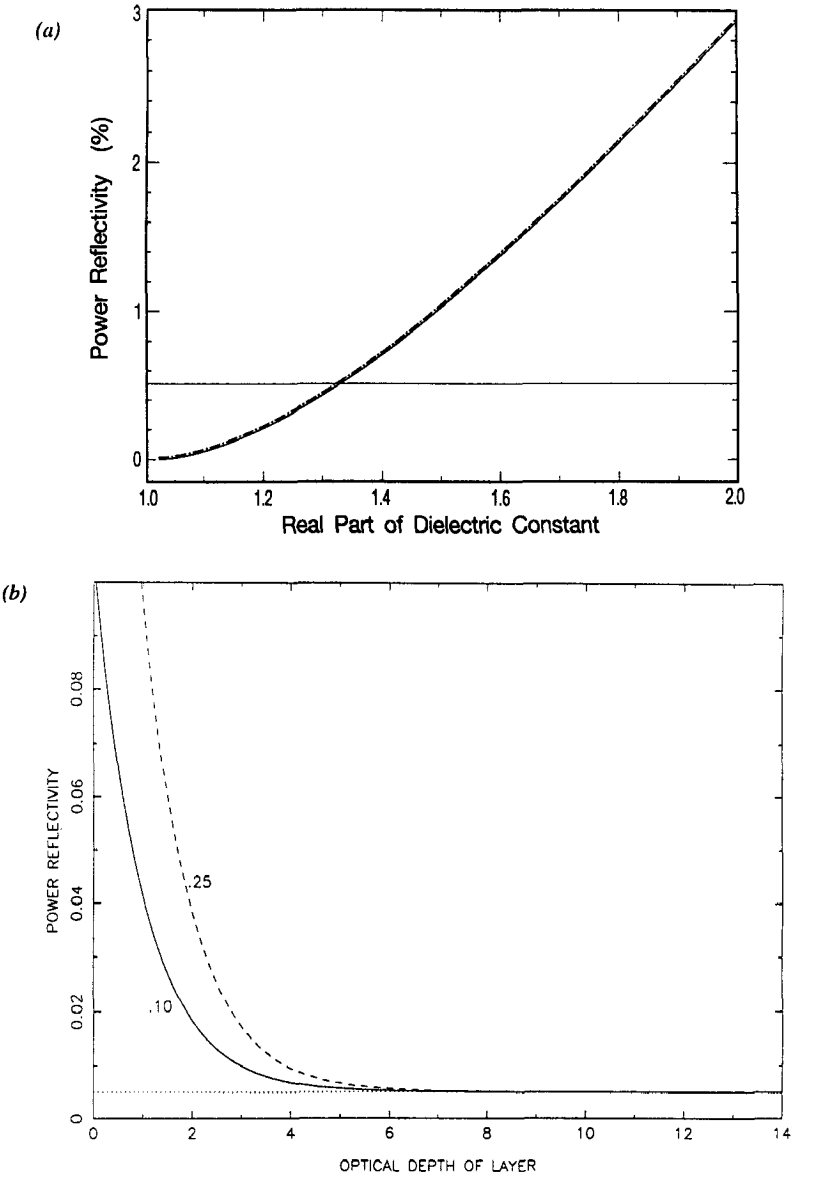

Figure 3 Reflectivity model for Stealth. (*a*) The normal incidence reflectivity for an infinite half-space of a homogeneous dielectric medium with the real part of the dielectric constant. A range of imaginary parts is shown with the dashed line. (*b*) The normal incidence reflectivity of a layer over the averaged Mars surface as a function of the 3.5-cm optical depth of the layer. Dotted and dashed lines indicate a wide range of absorption coefficients.

It can be seen from the figure that for reasonable values of the Martian sublayer reflectivities of 10 and 25%, the 3.5-cm optical depth must be greater than 5 or 6 to be consistent with the observations. Complimentary observations from Arecibo at a longer wavelength (13 cm) should make it possible to better estimate the minimum depths. A reasonable interpretation of this opacity has yet to be offered.

It is well known that the electrical absorption coefficient for amorphous and crystalline solids (nonmetals) is given by

$$k_v = \frac{2\pi}{\lambda}\sqrt{E_r}\tan(d), \tag{3}$$

where λ is the wavelength in the same units as D and $\tan(d)$ is the loss tangent of the material. Then from Equation (1) with $\tau \geq 5$, the minimum depth D can be estimated for reasonable values of $\tan(d)$. Such values for estimates of the complex dielectric constant of Martian soils are given in Paper I based on laboratory measurements tabulated by Campbell & Ulrich (1969). For example, a soil made by grinding a "typical" Earth basaltic rock to a density of about 1.0 gm cm^{-3} would have an $E \sim 2.0 - i0.016$ (see also Muhleman & Berge 1991 for further discussion). Such a soil packed with density of 0.4 gm cm^{-3} would possess $E \sim 1.33 - i0.0043$, a reasonable estimate of what is expected for Stealth. Using this value and Equations (1) and (3), we estimate a minimum depth of $D \sim 7.5$ meters for the layer. This hypothetical basalt is actually strongly absorbing. Following Paper I, the value for a less mafic soil that is certainly within the expected range for Mars is $E \sim 1.33 - i0.00215$, which for $\tau = 5$ gives $D \geq 15$ m. These calculation are highly idealized, and the uncertainties of the measurements suggest the minimum depth of the under dense layer could be as small as 2 or 3 m.

Our estimates of 7–15 m for the Stealth deposit (with density $\sim$ 0.4 gm cm^{-3}) are nearly as remarkable as the lateral extent of the deposit. Nothing like this exists on the Earth or is known to exist on the terrestrial planets or the Moon. The fact that the deposit lies to the west of the colossal Tharsis volcanic ridge in the equatorial zone is very significant. Furthermore, the topography falls from the eastern boundary at about 8 km above the Mars reference datum to near 0 km at the western boundary. *Viking* images of the ensemble of regions making up Stealth have been studied by many investigators including Scott & Tanaka (1982), Carr (1984), and Schultz & Lutz (1988). The geological map of Scott & Tanaka (1986) shows that much of the eastern and northern parts of Stealth lies in the upper and middle Medusae Fossae units. The east/west division in the feature is related to the Mangala Valles region, which is a cratered area somewhat elevated relative to Medusae Fossae units. Most of the southern boundary of Stealth is labeled as "Highland-Lowland Boundary Scarp" in the geological map. Scott & Tanaka have interpreted these units as ash-fall, ash-flow tuff, or thick eolian deposits. This interpretation was adopted by Muhleman et al

(1991), who suggested further that the ash flow may have originated from the Tharsis ridge volcanoes Arsea and Pavonis Montes. These volcanoes are situated in the equatorial zone where the prevailing winds are thought to be from east to the west, similar to the tropical trade winds on Earth. This is consistent with the general circulation calculations of Pollack and others. However, if the depths suggested here are correct, the materials must possess significant strength against collapse. Roughly, a 7-m column of material at density 0.4 gm cm^{-3} would have a base pressure of 280 gm cm^{-3} and cannot be "dust" and may be in a welded form like pumice. Finally, it should be noted that the entire Stealth region has been mapped as a region with very low thermal inertias; see Kieffer et al (1977) and Palluconi & Kieffer (1981).

Tharsis Volcanic Region

The Tharsis region includes the three shield volcanoes on the Tharsis Ridge: Arsia, Pavonis and Ascraeus Montes, and Olympus Mons—all structures of order 25 km above the datum level of the planet. These, and a number of other "old" volcanoes, surround the north and east boundaries of Stealth. In addition to the number of known remarkable characteristics of these structures, the VLA/Goldstone images reported in Papers I and II revealed important new facts about the region. All four volcanoes have distinct radar features that are nearly the brightest on the planet, after that of the Residual South Polar Cap, so evident in Figure 1. Equally radar-bright are regions in the Elysium complex discussed below. Butler (1994) has developed a useful technique for combining the data from all of the snapshots in which a given feature is visible. A feature near the equator is imaged over a wide range of look angles—angles of incidence combined with the local azimuth angle toward the radar. He has assumed that the backscatter intensity for a given point on the surface can be represented by the simple function

$$I(\phi, x, y) = A \cos^n \phi, \tag{4}$$

where ϕ is the incidence angle at time t, and x, y are the surface coordinates of the point. The reflectivity data for a given point were fit in a least-squares sense by adjusting A and n in Equation (4). A takes on the meaning of the reflectivity that would be observed at normal incidence at that point. The intensity I is effectively averaged over a pixel area in the final composite image of the resulting values of the parameter A, which are then normalized to reflectivity units. One such composite map (for Stealth) is shown in Figure 2. Information is lost in this manner because an average has been taken over a range of azimuthal angles. A cylindrical projection of the SS data for the entire Tharsis and Elysium domains is shown in Figure 4. The shields and calderae of the major volcanic structures from photographic images and geological maps are indicated by white lines in this figure. The reflectivities (which are really values

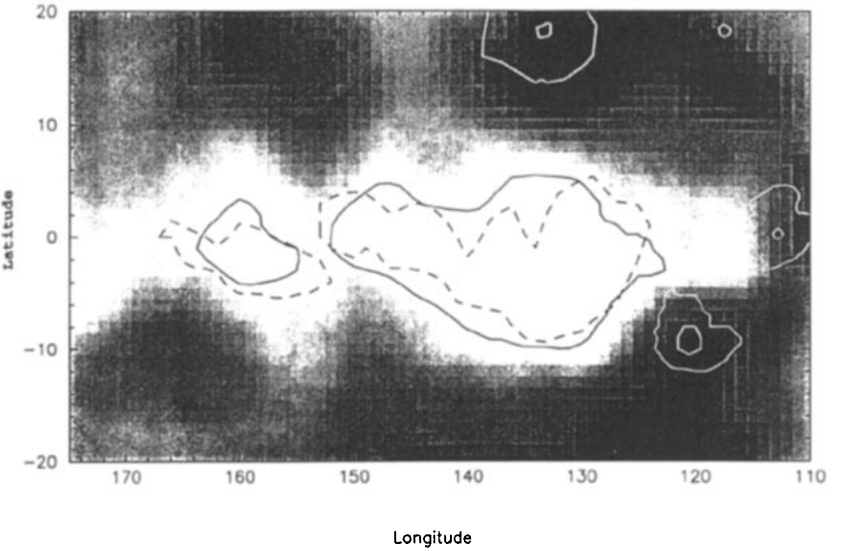

Figure 4 A cylindrical projection of the SS reflectivity of the entire Tharsis and Elysium regions. The contours are in 2.5% increments and the gray scale runs from −.4 to 24.6%. (From Butler 1994.)

of A_{SS}, the reflection coefficient at normal incidence for SS polarization) are indicated both in gray scales and contour lines. A number of things are noteworthy in Figure 4. The low reflectivity region containing Stealth continues westward to south of the Elysium complex (roughly centered at 210°W, 20°N). All of the bright radar features are associated with the volcanoes, including the largest region in Daedalia Planum centered on 122°W, 21°S (called the "south Tharsis" in Paper I). Only the bright feature in Ascraeus Mons falls on the mapped position of the caldera, while the bright feature in Arsia Mons is on the edge of its caldera. These structures are more closely examined in the next paragraphs.

The details of Arsia Mons can be seen in the A_{SS} map in Figure 5*a*. The dominant feature in this map is the huge anomaly directly south of the breach in the Arsia Mons caldera. The brightest pixels in this map have normal incidence reflectivities of $A_{SS} = 24.6\%$ and $A_{OS} = 22.7\%$ (at 122°W, 21°S) (Paper II). These values should be compared to the the Martian mean values for the globe excluding the radar anomalies. When extrapolated to normal incidence these values become $A_{SS} = 1.5\%$ and $A_{OS} = 4.0\%$, with a ratio of 0.37. The *Viking* images of this region (see p. 234 of Tyner & Carroll 1983) show that it is heavily grooved toward the southwest direction from the volcanic breach. It is tempting to interpret this grooved terrain as fresh lava flows because of its relationship to Arsia Mons, its extreme roughness, and its very high reflectivity. We know of no structure on the terrestrial planets or the Moon that approach these values except

for the ice on the Residual South Polar Ice Cap (RSPIC). Some ground truth does exist from Earth lava flows but these have considerably smaller numerical values (see Campbell et al 1993 and the references therein). Of course, we cannot define the word "fresh," but the results strongly suggest that the reflections are created by both maximum roughness, and possibly, by highly metallic lavas. The reflectivities near the caldera on Arsia Mons are also impressive with $A_{SS} = 15.8\%$ and $A_{OS} = 13.0\%$ at 120°W, 9°S (we doubt that the difference in these values is significant). Quite consistently, the polarization ratios in all the volcanic anomalies is near, or slightly greater, than unity. Although such values are possible for surface reflections from blocks whose random

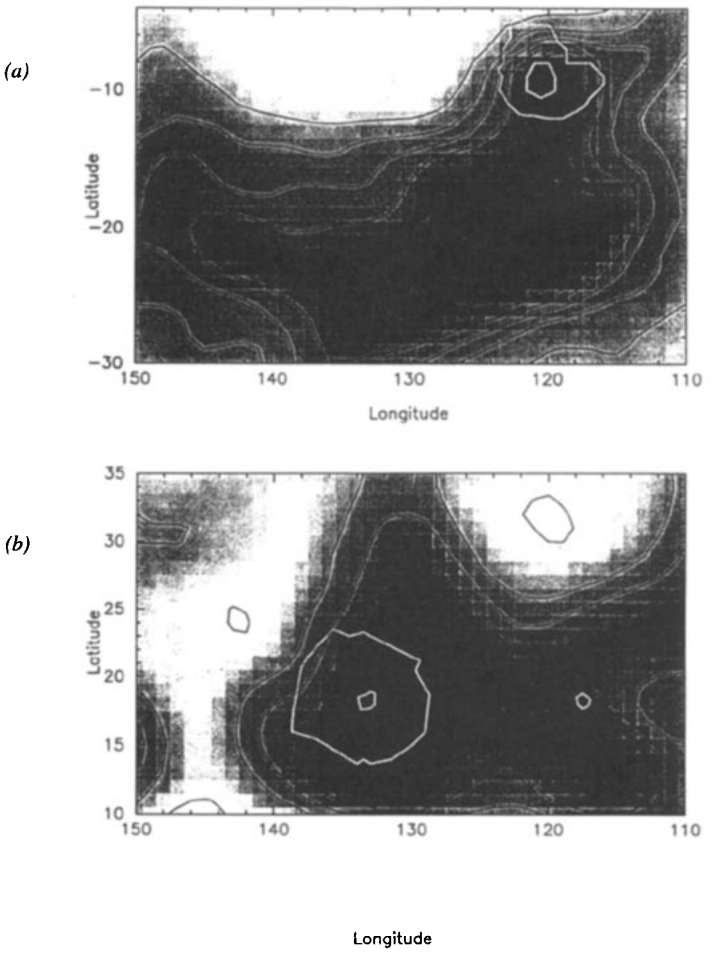

Figure 5 (*a*) Cylindrical projection of SS reflectivities for Arsia Mons. Contours and gray scales are the same as in Figure 4. (*b*) Same for Olympus Mons region, but the gray scales range from 2.25 to 17.4%. (From Butler 1994.)

orientations create good corner reflectors, they more likely result from multiple scattering of energy penetrating into the surface. The *Viking* images of Arsia Mons show nothing of obvious interest at this location (Tyner & Carroll 1983, pp. 238–39); however, the radar feature does lie on the back wall of the caldera.

The feature in Ascraeus Mons, which is even brighter, falls right in the caldera ($A_{SS} = 34\%$ and $A_{OS} = 22.7\%$ at 104°W, 11°N). The *Viking* images, (Tyner & Carroll 1983, p. 128) suggest that the caldera is strongly broken or is the superposition of a number of calderae. Again, the fundamental question is: How recent was the last volcanic activity? The complexity of the reflection physics and the lack of ground-truth data make it very difficult to interpret these results. The radar anomalies on Olympus Mons ($A_{SS} \sim 17\%$) and on Pavonis Mons ($A_{SS} \sim 20\%$) are on the flanks of these volcanoes and are also strong scatterers. Apparently, these were created by more recent volcanic activity than that in the calderae, although the structure and texture of the lavas may have been different at the time of the flows. The Pavonis anomaly is on the edge of the volcano's shield, and its caldera is only moderately more reflective than the mean in Tharsis. The cylindrical projection of the A_{SS} values for Olympus Mons is shown in Figure 5*b*, where the photographed outline of the volcano is indicated by white lines. The two brightest features are essentially off the shield although the caldera is moderately bright. The feature centered on 117°W, 14°N is actually on the west flank of the Tharsis ridge and may not be associated with Olympus Mons.

Elysium Complex

The Elysium complex was poorly viewed in the 1988 VLA/Goldstone experiments and was properly imaged in 1993. The 3.5-cm radar map appears in Paper II and is reproduced here in Figure 6. Again, the radar anomalous regions tend to be adjoining the principal volcanoes with a peak SS reflectivity of $A_{SS} = 20\%$ (203°W, 20°N). The Elysium caldera is at 214°W, 25°N and, although there is no doubt that it is part of Elysium Mons, it may be incorrect to closely associate the radar anomaly with this volcanic complex. The caldera extends southeast from the volcano down the Elysium rise. Harmon et al (1992a) obtained images at Arecibo at 13 cm in 1990 and have published a single SS image of the Elysium quadrant. They used the new long random code technique to image the surface without aliasing. The maps are in good agreement, and the major differences may be due to the different way the data sets were projected. In particular, the Arecibo map suggests higher reflectivity than the VLA map in the region called the Cerberus Formation by Plescia (1990). This structure covers the region from the equator to about 10°N and is roughly bounded between 180°W to 210°W. Harmon et al observed a bright, nearly linear feature in the northeast corner about 500 km long, which is prominent in Plescia's map but not in the 3.5-cm data as projected in Figure 4.

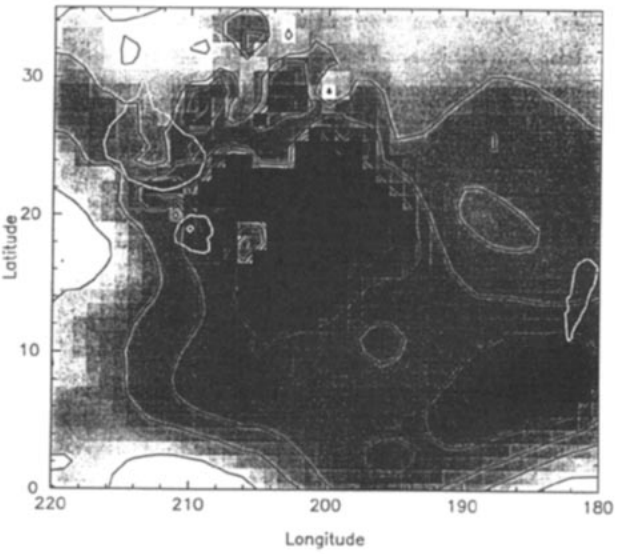

Figure 6 A cylindrical projection of the SS reflectivities in the Elysium region. The contours are at 2.5% increments and the gray scale ranges from 1.5 to 20.3%. The white lines suggest the calderea flanks of Hecates Tholus to the north, Elysium Mons in the center, and Orcus Patera to the east. (From Butler 1994.)

The Arecibo group points out the close correspondence of their 13-cm map with the Cerberus Formation, which has been interpreted as a floodplain deposit; the more sinuous linear feature to the east is decribed as a "smooth-floored outflow channel" by Tanaka & Scott (1980) (see also Carr & Clow 1981). Harmon et al (1992a) conclude that there is general agreement in the geological literature that the "Elysium Basin was the site of a paleolake and that the channel was an outlet for water flowing northeast into Amazonis." However, this seems in clear conflict with the radar-brightness of the region at both 3.5- and 13-cm wavelength, which is very likely associated with lava flows and deposits. Plescia (1990) has interpreted this region, including the channel, as having been flooded by low-viscosity lava flows, postdating the fluvial episodes. This scenario is consistent with the radar data. The absence of clear evidence for the channel in Figure 4 at 3.5 cm is puzzling. While it may be a projection defect in the mapping, the possibility exists that other reflection mechanisms are operating if, indeed, the 13-cm reflections are significantly stronger. That could occur if the enhanced reflections were caused by volume scattering from buried rocks or lavas because the long wavelength energy could probe to 2–3 times the depth of the 3.5-cm signals in partially transparent materials such as very dry "sand."

Polar Regions

The first radar images of ice on Mars were made from the VLA/Goldstone 1988 observations when the subradar point on Mars had a latitude of 24°S and the Martian longitude of the Sun was $L_S = 295°$ (mid-southern summer). Six of the 38 snapshot images are shown in Figure 1 where the prominence of the south polar ice reflection is obvious. The SS reflectivity at the angle of incidence 66° was reported to be essentially unity in Paper I and has been corrected to 85% in Paper II and in Butler et al (1993), hereafter called Paper III. The necessary correction factor of $\frac{1}{2}$ brings this value to 42%. The pixels with the very large reflectivities all lie on the RSPIC as seen in *Viking* and *Mariner 9* photographs. This ice deposit behaves like a "white" screen, even at angles of incidence near grazing. This requires the ice to be heterogeneous with cracks, voids, or condensations acting as scattering centers. The data were interpreted as the reflection from a multiply scattering medium, which is essentially conservative at centimeter wavelengths, i.e. with a single scattering albedo essentially unity. The strong backscatter at grazing incidence angles was a surprise because it was expected that the ice (either water or carbon dioxide) would be homogeneous, either from annealing processes or ab initio as the ice was laid down in the form of frost. It was also shown in Paper I that the medium is essentially transparent and that scattering from rocks in the ice matrix could be ruled out, consistent with conservative scattering.

The polar data were remapped by averaging the data from the snapshots, and the results for both the SS and OS data are shown as radar cross sections in Figure 7. The SS cross sections are nearly twice as high as the OS values for the pixels on the RSPIC, which are marked with white lines. (SS values also exceed the OS values in a kind of penumbra around the visible ice cap, caused by the projection technique.) The anomalous polarization ratios are also found on the icy Jovian satellites as discussed earlier and appear to be a clear indicator of planetary ice, or at least, the presence of highly transparent material at the relevant wavelength, such as very cold ice. Even the minimum thickness of the ice is nearly impossible to estimate with such meager data. The problem was modeled as a pile of spherical ice balls in Paper I, yielding a minimum thickness of about 1.6 m for ice spheres the size of the wavelength piled on top of each other. It was also modeled in Paper I as a suspension of such scatterers in a transparent matrix, yielding about a 5-m thickness for separations of about 25 cm between the scattering centers, an arbitrary value. The problem was modeled somewhat more accurately in Paper III using a power-law size distribution in a similar Monte Carlo calculation. It was concluded that for the epoch of observation the minimum thickness would have to be about 10 m if the Martian dust contamination of the ice was about 1%. The data and interpretations clearly establish that the upper few meters of the ice sheet are remarkable clean and very heterogeneous, i.e. highly fractured or lumpy. It is

not at all clear why the ice on Mars is in this state, but annealing calculations reported in Paper III show that once the ice (assumed to be water) is in that state at the Martian poles, it will remain that way.

The north polar region has only been observed at the VLA and at a time when the grazing angle at the pole was just 9° to 6°, dangerously low to observe the effects of the Residual North Polar Ice Cap (RNPIC), which is much more extensive than the RSPIC. The season was early spring with $L_S = 18.2°$ and 24.8°, respectively—perhaps early for the sublimation of the seasonal CO_2 ice cap. The seasonal cap is estimated to be of order 1 m thick and should be essentially transparent to 3.5-cm energy even at an incidence angle of 81°. However, the radar signature for ice was not seen! Cross-section images from Papers II and III are shown in Figure 8; the boundary of the RNPIC is indicated in white. Even though the RNPIC extends down to about the 80°N latitude circle where the grazing angle reaches about 18°, no reflectivity enhancement due to ice is present. The putative ice deposits on Mercury were detected at a grazing angle of 13° as discussed below. Butler et al offer in Paper III several possible but unconvincing explanations for the newly found dichotomy between the two poles.

1. The grazing angles are too low for the RNPIC; the RSPIC was observed at 24°.

2. The seasonal CO_2 frost was still in place and tended to fill the voids, removing the heterogeneous dielectric structure.

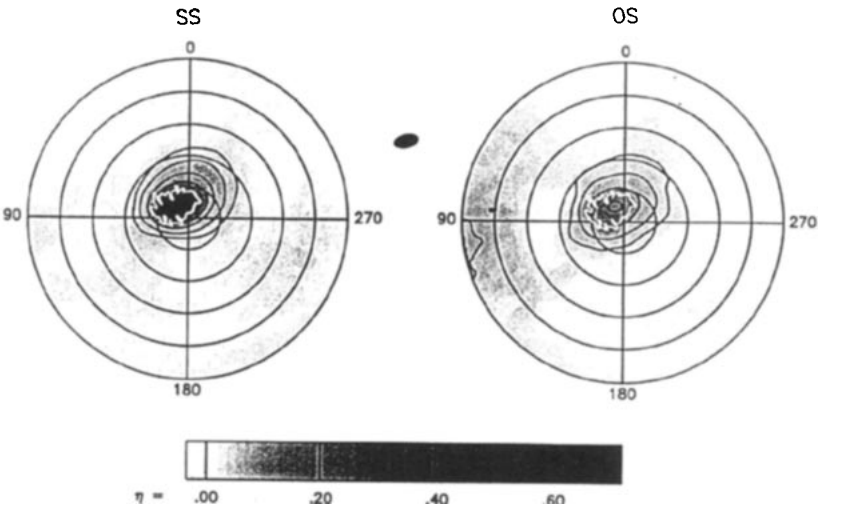

Figure 7 Stereographic projection of the south polar SS (*left*) and OS (*right*) cross sections. The contours are at reflectivities = 0.025, 0.05, 0.1, . . . , 0.4. The white lines represent the Residual South Polar Ice Cap. $L_S \sim 295°$. (From Butler 1994.)

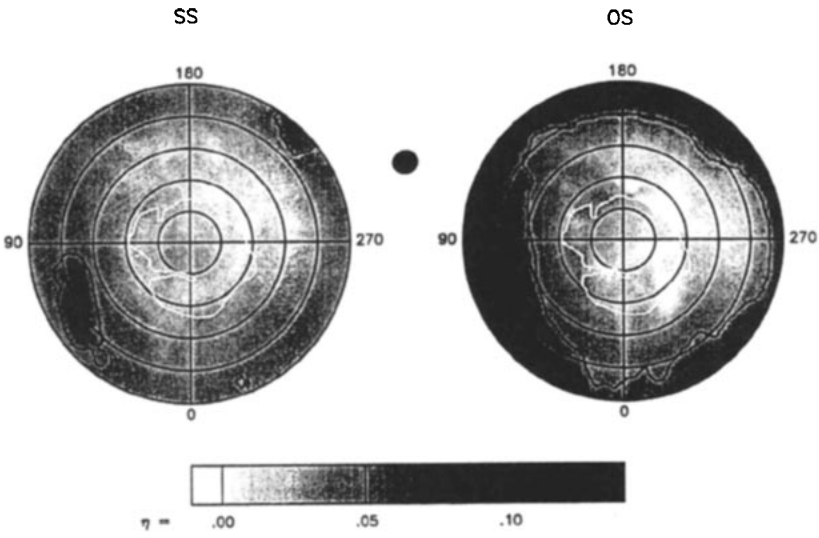

Figure 8 Stereographic projection of the north polar SS (*left*) and OS (*right*) cross sections. The contours are at reflectivities = 0.025 and 0.05. The white lines represent the Residual North Polar Ice Cap. $L_S \sim 20°$. (From Butler 1994.)

3. The seasonal dust deposition in the north was sufficient to raise the absorption properties of the matrix above a critical value to turn off the coherent backscatter effect.

4. The thermal environment at the north pole is sufficiently different from the south pole to allow much more efficient annealing of the ice fractures. For example, our knowledge of the topography at the poles is very poor but is likely to be relevant.

5. The glacier-like ice flow is significantly different in the north than in the south. The ice could be more loaded with soil and rock debris, thereby creating more absorption.

This important problem remains unsolved and none of these mechanisms seems to be sufficiently robust to explain the striking observational dichotomy. Better measurements such as those promised from the ill-fated *Mars Observer* mission are required.

Radar astronomy of Mars has been a fountainhead for information about the planet and will continue to be important. Much higher resolution can be achieved on Mars with the VLA/Goldstone radar. The observational technique using 12–15 minute snapshots was dictated by signal/noise considerations in the selection of the observing Doppler bandwidth. If a significant increase in transmitter power at Goldstone were achieved, narrower channels at the

VLA could be employed with increased east/west resolution, e.g. 2–5 minute snapshots might be possible. The use of the long-code techniques at Arecibo (and with Goldstone in the monostatic mode) will yield more interesting Martian maps, albeit, always plagued by the north/south ambiguity about the Doppler equator. At the time of this writing, the transmitter power at Arecibo is being significantly increased to 1 MW, and the surface will be considerably improved. The increase in the resolution of radar maps will be impressive. Finally, the radar globe of Mars is certainly different from the photographic globe because of the penetrating power of microwaves. It certainly can be argued that a *Magellan*-like mission to Mars would be very fruitful! Interestingly, we do not have a photographic globe of Venus.

MERCURY

Mercury was first observed with the Goldstone radar by Carpenter & Goldstein (1963), observations both in the form of Doppler spectra and somewhat crude range-gated spectra with range depths of 178 km. These observers missed detecting the striking result that Mercury was not in synchronous rotation with its orbit about the Sun (87.97 day period) but was in a faster rotation with a period of about 59 ± 5 days, which was discovered at Arecibo by Pettengill (apparently first reported in Pettengill 1965). This result produced a flurry of theoretical work by G Colombo, II Shapiro, P Goldreich, and S Peale, which resulted in the realization that Mercury's solid body rotation was locked in the $\frac{3}{2}$ spin resonance with its orbital motion and that the spin axis is very nearly perpendicular to its orbital plane (see the review by Peale 1988). Unfortunately, the rotation period of 59 days means that Mercury spins too fast for range-gated Doppler mapping to work well, and the planet remained essentially unmapped until the first VLA/Goldstone radar imaging experiment on August 8, 1991. Of course, half of the surface of Mercury was photographed with resolution of a few kilometers from *Mariner 10* in 1974 (see, in particular, Murray et al 1974). The *Mariner* results have been widely distributed in map and book forms such as Davies et al (1978). The entire globe of the planet was imaged with the VLA/Goldstone radar at a wavelength of 3.5 cm. Four such images are shown in Figure 9. Figure 9*a* was the first image obtained (on August 8, 1991) when the north pole was tilted toward the Earth by 10.7°. At this angle the line of sight was down into the north pole and the brightest echo from the planet was around this pole. The striking similarity between the images in Figures 9*a* and *b* (obtained 15 days later) with the images of Mars shown in Figure 1 was immediately suggestive of ice on the north pole of Mercury.

Mercury's position as the innermost planet in the Solar System is sufficient to make it unique since it presumably formed nearest the Sun. It has no satellite and has evolved to a simple rotational state with its spin axis exactly perpendicular to its orbital plane to the accuracy of the measurements. If Mercury were a

smooth sphere, the Sun would never set on any point on the globe. A crescent Sun, modulated by the varying solar distance, would always be seen from the poles. However, the bottom of any crater exactly at the pole will be in perpetual shadow, warmed only by light scattered from the crater rim, heat conducted up from the planet's interior, and cosmic "light." Estimating just how cold these spots could be is very difficult and depends on the details of the crater, but temperatures as low as 30 K are possible. Temperatures on the Mercury nightside fall to about 90 K at the very surface. Craters known from *Mariner 10* imaging of the then dayside of the planet would have permanently shadowed zones if they lie within about 5° of the pole and possibly even further. Cold traps for volatiles are also created on the poleward sides of ridges and certainly in cracks within about 10° from the poles.

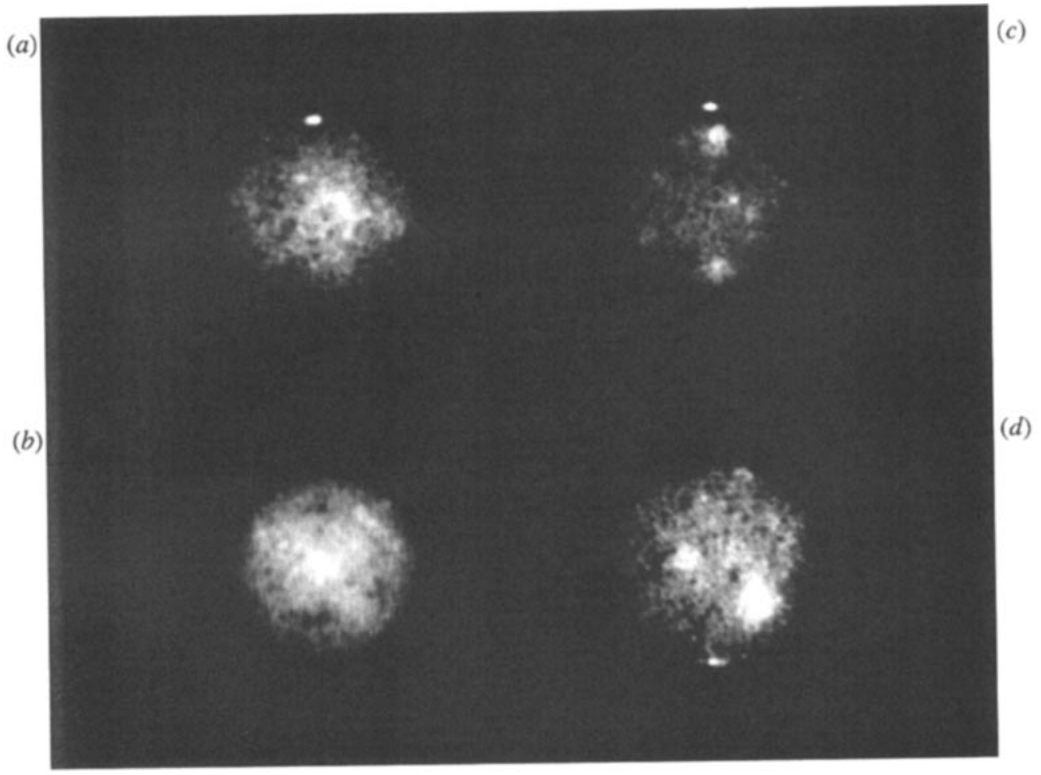

Figure 9 Radar SS images of Mercury at four epochs: (*a*) April 8, 1991 with the north pole tilted toward the Earth, (*b*) April 23, 1991 with the north pole tilted toward the Earth, (*c*) November 23, 1992 with the subearth point nearly on Mercury's equator (−2.3°), and (*d*) February 21, 1994 with the south pole tilted toward the Earth. (Copyright: BJ Butler, DO Muhleman, and MA Slade, 1994.)

The maximum angle that the solar limb rises above the poles is just 0.9° and sunlight illuminates the wall of an ideal polar crater by this small angle. However, the orbital plane of Mercury is inclined to the Earth's orbital plane by 7°, causing the line of sight between the planets to be inclined to Mercury's equator by up to 13.2°. This makes it possible to look down from the Earth into the polar regions by this angle, revealing a small but significant part of the permanently shadowed terrain from the Earth. The maximum viewing angle achieved during the last quarter of the twentieth century was 11.6° in August, 1991 when the Caltech/JPL group was imaging Mercury with the VLA/Goldstone radar. The brightest radar feature on the planet was contained in a circle about the north pole with a diameter of about 300 km, confined within the 86.8°N latitude circle. The images in Figures 9*a* and 9*b* were created at that time. The image in Figure 9*d* was made on February 23, 1994 when the subearth angle on Mercury was −10.6°. A polar feature is again obvious, this time in the south. The image in Figure 9*c* is closer to the view from the Sun and the polar features are not visible at the polar grazing angle of −2.3°.

The VLA/Goldstone observers immediately concluded that the polar radar feature was most likely explained by deposits of ice in the permanently shadowed regions around the north pole, and they published this speculation in Slade et al (1992). The discovery was confirmed within days at Arecibo and reported by Harmon & Slade (1992). Supporting thermal equilibrium calculations were published by Paige et al (1992). Armed with the knowledge of the north polar feature, Harmon & Slade (1992) found a very similar radar feature on the south pole in data taken earlier at Arecibo. As pointed out in Slade et al (1992), the ratio of the echo power measured in SS mode to power transmitted was about 1.5 times that measured in the OS mode, a phenomenon previously measured on the icy Jovian satellites by Campbell et al (1977) and on the Martian residual south polar ice cap by Muhleman et al (1991).

The evidence for ice on the poles of Mercury was immediately persuasive. The presence of very bright features confined to within a few degrees of both poles in regions where permanent shadowing must occur, possessing inverted polarization ratios, strongly suggests the condensation of a volatile in cold traps. The most likely volatile on Mercury is water. Butler et al (1993) presented theoretical calculations on the stability, mobility, and retention of water in the permanent shadows on Mercury, which required temperatures no lower than 120 K at the sites. More recent Arecibo observations of Mercury published by Harmon et al (1994) report a good correspondence between patches of ice-like reflectors and known craters from *Mariner 10* images. In particular, most of the south polar feature is in the crater Chao Meng-Fu, first suggested by Harmon & Slade (1992). Radar images of the north and south polar re-

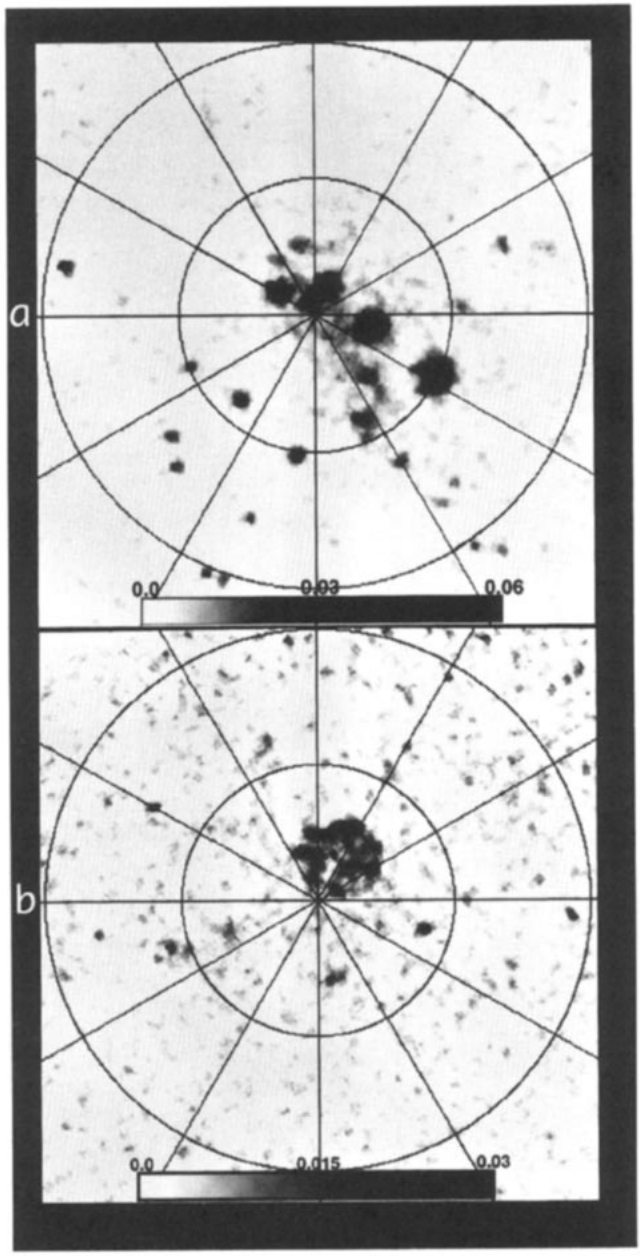

Figure 10 Radar delay–Doppler radar images of the (*a*) north and (*b*) south poles of Mercury at a wavelength of 12.6 cm from Harmon et al (1994). Latitude circles of 80° and 85° are shown.

gions from Harmon et al (1994) are shown in Figures 10*a* and *b*, respectively. These images are polar projections; they show that the bright spots in the north break up into discrete units, some of which the authors have associated with craters charted from *Mariner 10*. It seems clear that the features above the 85°N latitude circle are ice-like with inverted polarization ratios and the authors suggest that some at lower latitudes have similar characteristics. The south polar region appears to be much simpler in that the main features lie in the crater Chao Meng Fu. The data for Figure 10 were all taken at a grazing angle of about 10° and it was not possible to see all of the ice deposits. Harmon et al (1994) also showed their features superimposed on the *Mariner 10* polar images. These are reproduced in Figures 11*a* and 11*b*. The radar features on the *Mariner 10* side are labeled with letters and line up very well with the darkened craters suggested by their bright rims. Similarly, Figure 11*b* shows the identification of Chao Meng Fu and several other small craters with the "ice" features. Thus, the case for volatiles in the permanently shadowed features near the poles is very compelling. The model calculations of Butler et al (1993) and those of Paige et al (1992) present highly plausible arguments that the volatile is indeed water ice. Temperatures below 120 K in the permanent shadows are to be expected and are sufficiently low that the ice is stable against sublimation for billions of years. Apparently, adequate sources of water on Mercury are supplied by meteoritic impacts, an occasional comet impact, and possibly, outgassing from the interior. Most of the water vapor near the surface of the planet is forever lost by photodissociation, but a significant fraction of the water molecules will random walk to the polar cold traps (Butler et al 1993).

Only a fraction of the putative ice can ever be observed from the Earth because of the poor geometry. It is highly unlikely that the ice can be imaged in active visible light because the deposits are probably covered with a layer of dust that could be as thick as 10 or 20 cm and still be transparent at radar wavelengths. The deposits can be sounded with a dual polarized radar system flying near the poles either with flybys or in Mercury orbit. Polarization ratios are diagnostic of nearly transparent reflecting media, and the presence of hydrogen atoms in the ice can be detected with a neutron spectrometer flying within a few hundred kilometers of the poles. While the presence of water ice in the shadowed regions is nearly certain, the ices of carbon dioxide and possibly ammonia, HCN, and SO_2 may also be present. Since the deposits are most likely as old as the craters on Mercury, they probably retain a chemical record of the inner Solar System.

Nearly all the structure seen in Figure 9 is real, and several anomalous regions other than the poles can be seen. First of all, the absence of a strong radar feature at the position of the Caloris Basin should be noted in Figure 9*c*. Caloris lies at about 2 o'clock, about $\frac{2}{3}$ out from the subearth point, and no basin-like feature

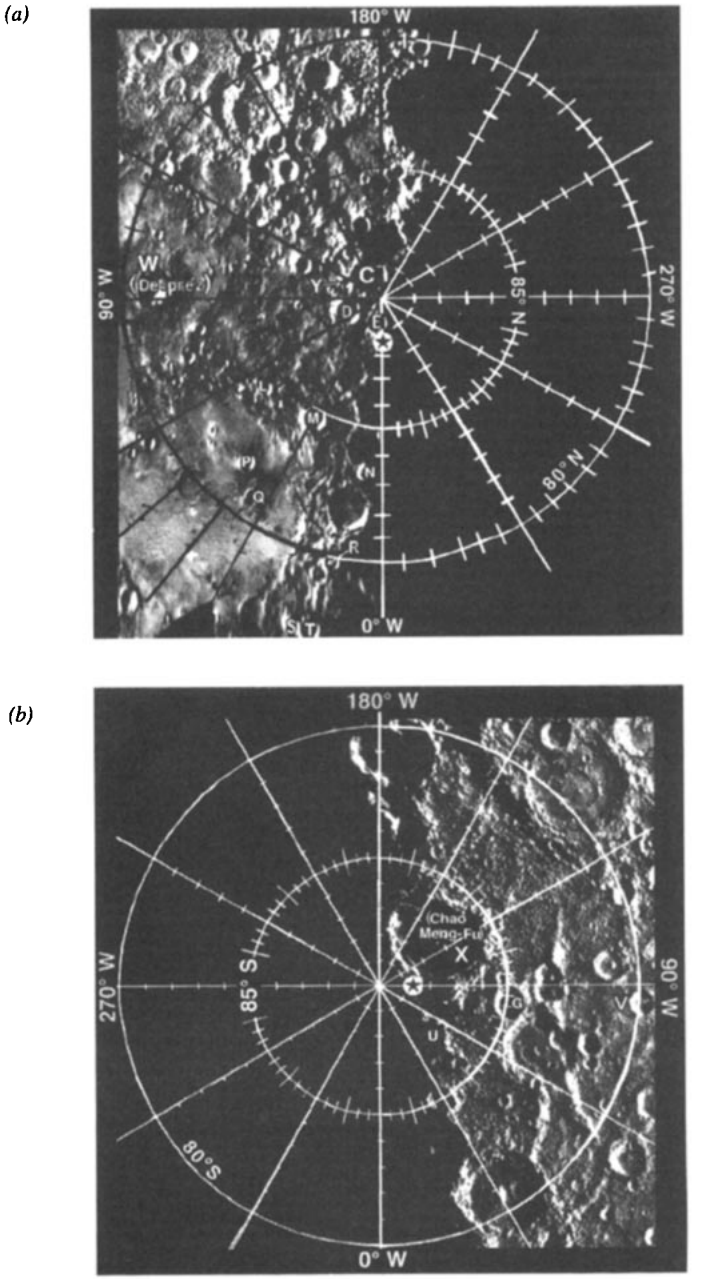

Figure 11 Superposition of 12.6-cm Mercury polar features over *Mariner 10* photographic images, limited to the hemisphere of Mercury imaged: (*a*) north pole, (*b*) south pole. The *Mariner* images have been slightly translated. (From Harmon et al 1994.)

can be seen although there is apparently a slight enhancement in the region. Two large anomalies are obvious in Figure 9*b*, just to the astronomical west (right) of the central meridian. The southern feature is better seen in Figure 9*d* where it is rotated to lower incidence angles. The next brightest anomaly is in the region containing the bright rayed crater Kuiper, well imaged by *Mariner 10*. The radar anomaly is best seen in Figure 9*d*, just east of the subearth point. We limit our discussion to just these three features: the Kuiper region and the North and South Radar Basins.

Radar SS cross sections of the Kuiper region and a *Mariner 10* image to the same scale are shown in Figure 12. A circle representing Kuiper itself is indicated in Figure 12*a* along with the very bright contours relative to the surrounding terrain with about 1.5% cross section at the angle of incidence

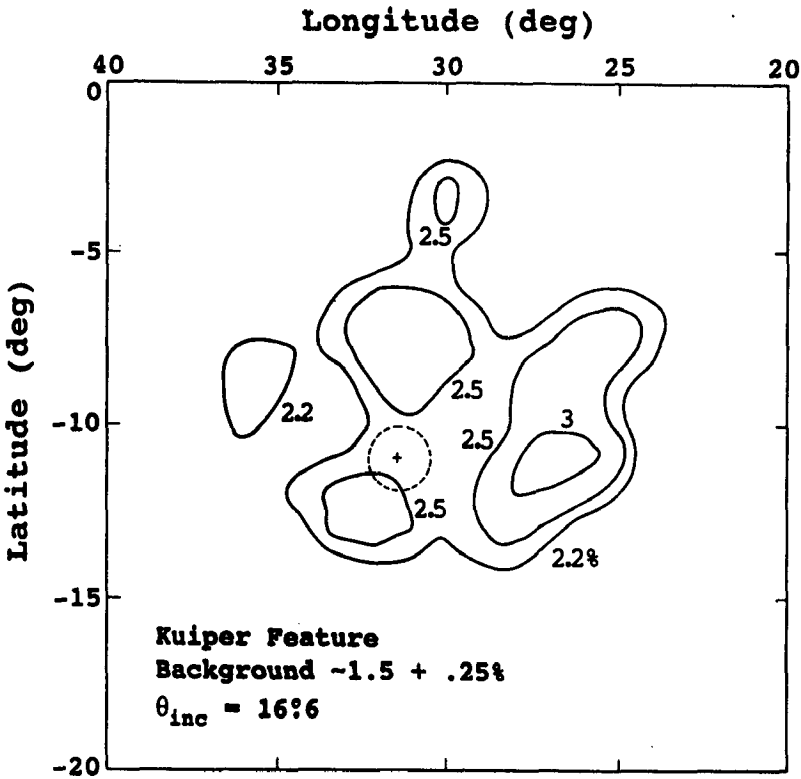

Figure 12 The Kuiper region on Mercury. (*a*) Contour lines of the SS reflectivity in a cylindrical projection. The surrounding region has an average SS reflectivity of ~1.5%. The Kuiper crater is indicated by the dashed circle. (*b*) A *Mariner 10* image of the Kuiper region to the same scale as that in (*a*).

at Kuiper of 15.6° (the data have not been corrected for a scattering law). The brightest feature is not on the crater but lies about 160 km to the east in what looks like rough terrain in Figure 12*b*. Like Caloris, the bright Kuiper crater is not a strong backscatterer and may have a smooth floor and walls on the scale of the wavelength. The image resolution is about the size of the 3% contour in Figure 12*a* and we cannot expect to resolve an echo enhancement from the far (east) wall of Kuiper although the small 2.5% contour may be related to that phenomenon. Higher resolution radar imaging of the region is required to better understand the relationship between the visually bright impact crater and the radar anomaly. Kuiper is similar to Tyhco on the Moon but the radar anomaly associated with Tycho is much smaller than that of Kuiper.

Much larger still are the North and South Radar Basins. The North Basin SS contours are shown in Figure 13, taken from the August 23, 1991 image of Figure 9*b*. The image is a cylindrical projection and the angle of incidence from the subearth point to the brightest point in the feature is 44°. If the 2.5% contour is corrected with a cosine scattering law, it becomes 3.5% and

(b)

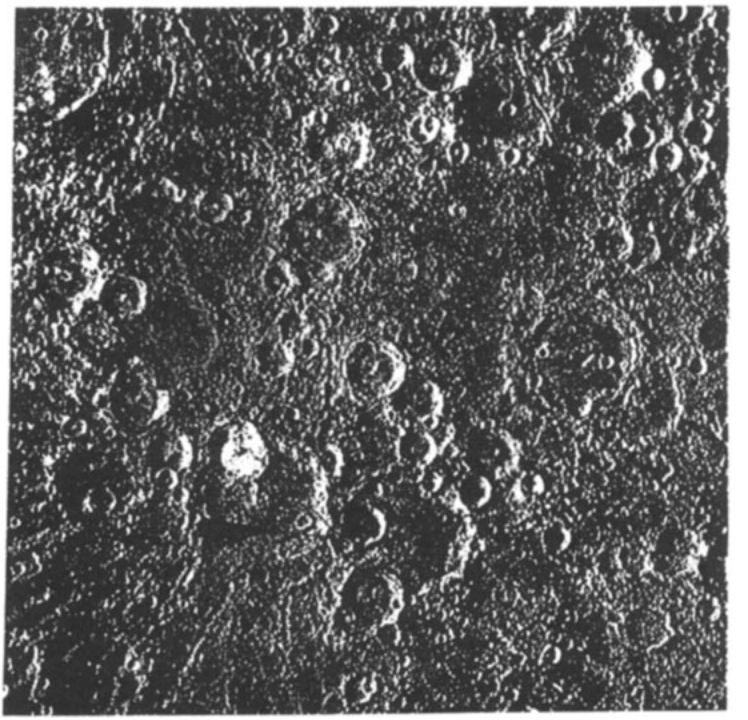

is both brighter and much larger than the Kuiper basin. The North Basin was well imaged in OS polarization. It looks very similar to the SS image with a polarization ratio of about 0.5 (Butler 1994), which strongly suggests that the basin is either extremely rough (blocky) or is a medium that exhibits nearly isotropic radar scattering [see Tryka & Muhleman (1992) for a discussion of such structures]. Unfortunately, there is no ground truth for this side of Mercury. The South Radar Basin is even larger, as shown in Figure 14, but has similar radar cross sections and polarization ratios. The feature is about the same size as the Caloris Basin but is extremely radar rough. Again, this may be caused by blockiness on the scale of the wavelength or may be a texture quality of the scattering medium. The centroid of the South Basin is located at about −29° south and about 349°W longitude, placing it near the antipodal point of the Caloris impact basin, which is roughly centered on 30°S and 15°W, as pointed out by Butler et al (1993). Hughes et al (1977) has suggested that seismic focusing of the Caloris event could have highly fractured the surface at the antipode. Such events could have conceivably created the scattering medium responsible for the radar basins.

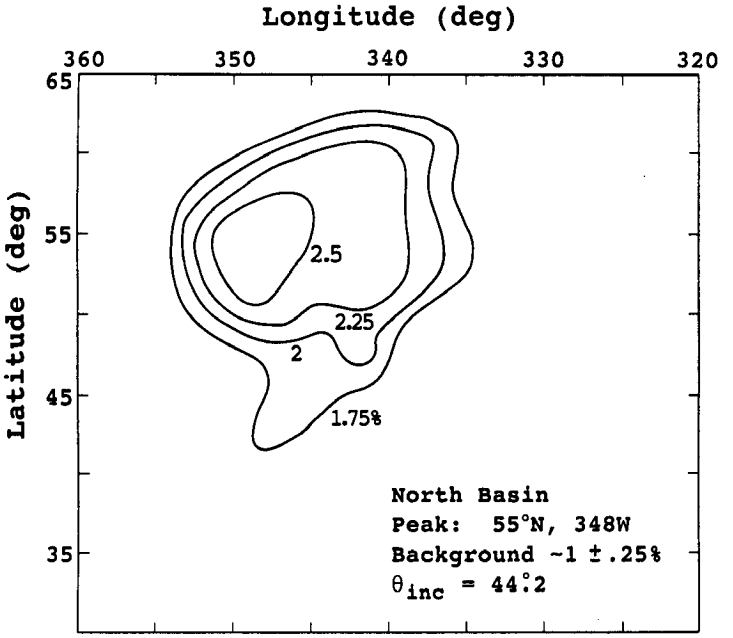

Figure 13 The North Basin radar feature. Contour lines of the SS reflectivity are shown in a cylindrical projection. The surrounding region has SS reflectivity ~1.5%. No *Mariner 10* images exist for this hemisphere.

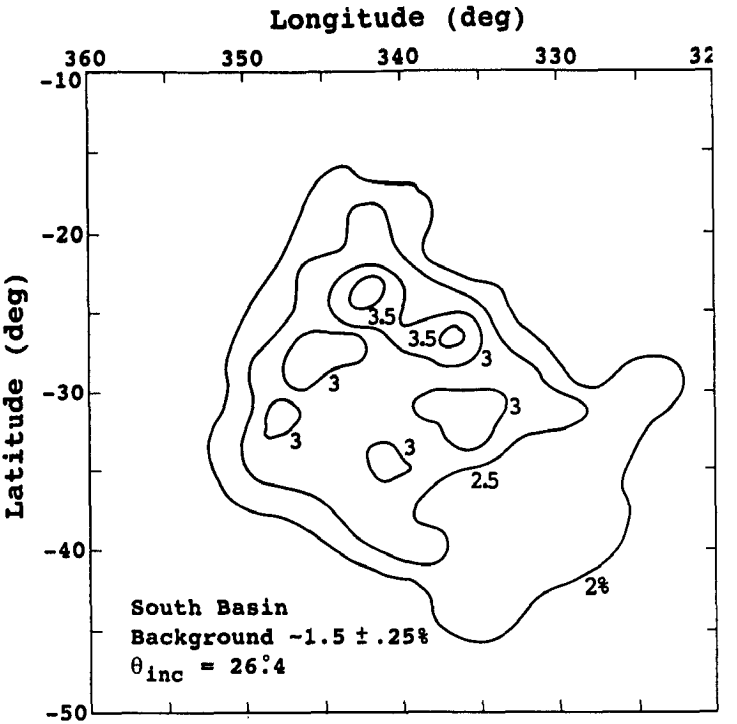

Figure 14 The South Basin radar feature. Contour lines of the SS reflectivity are shown in a cylindrical projection. The surrounding region has SS reflectivity ~1.5%. No *Mariner 10* images exist for this hemisphere.

TITAN

Titan, the largest satellite of Saturn, has taken on a central role in planetary science because it presents as many enigmas as any planet in the Solar System. Our current knowledge of the satellite is reviewed in Hunten et al (1984), and Lunine (1994) has written a recent review on the Titan atmosphere, focusing on central unanswered questions. Little is known about the surface of Titan because optically thick clouds and hydrocarbon aerosols completely obscure the surface from view at visual wavelengths. The atmosphere becomes transparent (opacity less than unity) at wavelengths longward of about 1 cm, although recent evidence suggests that there may be a partially transparent window near 1 μm, which allows some surface emission to be observed (see Griffith et al 1991 and Griffith 1993). Thus, the surface can only be imaged remotely with radar, although surface microwave emission averaged over the mean disk has been studied by Grossman & Muhleman (1995). Convincing theoretical arguments suggest that Titan's rotation is synchronous with its orbital period about Saturn

of 15.94542 days. However, both the period and the orientation of the spin axis remain unconfirmed by direct measurements. In principle, these quantities can be measured with radar techniques, given sufficient signal. Hubbard et al (1993), in the analysis of the massive data set from the occultation of 28 Sgr by Titan, reported that the upper atmosphere, though distorted by zonal winds of order 100 m sec^{-1}, "shows substantial axial symmetry" with a position angle of the axis within $\sim 1°$ of Saturn's. i.e. perpendicular to Titan's orbital plane. Such winds are super-rotational if the rotation period is 16 days.

Titan offers an extremely difficult radar target. In addition to being the most distant object detected by radar, during the past two decades the Saturn system has been deep in the southern sky at low declinations. It will not reach northern declinations near closest approach to the Earth until October, 1997. Thus, the source has been invisible to Arecibo and has had short transits over Goldstone and the VLA, amounting to a little more than twice the radar round-trip light-time of 2.5 h. At best, the full disk echo signal from Titan is 4.5 orders of magnitude weaker then Mercury's disk, not allowing for the much shorter integration times available for signal detection. The surface is expected to be composed of ices contaminated by solid and liquid hydrocarbons but essentially nothing is known about differentiation of heavier materials such as silicates and other meteoric material. The bulk density is 1.881 gm cm^3, similar to that of Ganymede and Callisto.

Echoes from Titan were first obtained in June, 1989 by Muhleman et al (1990) using the VLA/Goldstone radar configuration. The diameter of Titan (5150 Km) subtends an angle of just 0.89 arc sec at 8 AU, which can barely be resolved with the VLA in its largest configuration at a wavelength of 3.5 cm. Since only the 351 antenna-pair cross products are measured and not the total echo power in each of the 27 antennas, there is a serious loss in sensitivity and resolved measurements have not yet been made. If the rotational period is near 16 days, then the maximum Doppler spreading of the echo is about 1300 Hz. Additionally, if the surface is as radar rough as the icy Jovian satellites, the echo energy is expected to be broadly spread to the full Doppler width. The initial experiments determined that, indeed, the echo was broad and thus that the surface is radar rough (Muhleman et al (1990). Several attempts were made to detect the echo from Titan using the Goldstone monostatic radar, and a reasonable Doppler spectrum was obtained after averaging over several days, verifying the broad limb-to-limb spreading of the echo (RM Goldstein & RF Jurgens, private communication, 1992).

A major motivation for the Titan radar experiments was the putative global ocean of liquid hydrocarbons (ethane/methane) put forward by Lunine et al (1983). They postulated that a surface reservoir up to several kilometers deep was required to resupply the methane currently in the atmosphere, which is irretrievably destroyed by photodissociation. Furthermore, hydrocarbons such

as ethane, acetylene, and methane must condense out of the atmosphere below the cold trap at the tropopause and "rain" down on the surface. Such a global ocean was ruled out in the initial experiment because the strong echo detections were about an order of magnitude greater than what would be obtained from a surface of nonpolar hydrocarbons. Additionally, the nearly Lambertian radar scattering from the surface is strongly inconsistent with a smooth, liquid surface. Essentially nothing is known about Titan's topography except that the cutoff radius of two radio occultation chords on opposite sides of the satellite were identical to within 500 m (Lindal et al 1983).

The authors of this review have carried out VLA/Goldstone radar experiments near the time of each closest approach of the Saturn system since 1989, obtaining a number of clear results and some puzzling ones. Much of this work was presented in Muhleman et al (1993). Titan observations were made by operating the transmitter from the time of Titan rise at Goldstone to 2.5 h before its setting at the VLA, yielding about 5 h total observing time on Titan, except for about 10% overhead used to observe calibrator sources. Under the best conditions, when the transmitter was operating at a maximum of 450,000 W and the weather was dry at the VLA, the Titan radar spectrum was measured in 381-Hz channels with a signal-to-noise ratio of 3–5 in a 5-hour track, i.e. solid detections could be made but with only marginal measurements of surface properties. Furthermore, observations during 1989–1992 were complicated by what we now believe were occasional pointing errors as large as the half-power beamwidth of the 70-m antenna, which resulted in a decrease in the measured reflectivities. For example, a 30 arc sec pointing error would cause the measured radar cross section to be depressed to 0.8 of the correct value. There is no method to check the pointing while the antenna is transmitting and errors of this size and larger may have occurred during Titan experiments. As we show below, new antenna pointing curves for Goldstone were available for the 1993 measurements, and indeed, the result are more consistent from day to day. Nevertheless, we cannot rule out the possibility that the fluctuations in the early data are real and possibly caused by large "lakes" of liquid hydrocarbons or other inhomogeneities on the surface. Certainly, the largest of the fluctuations in the measured cross sections can not be caused by pointing errors and are probably real effects associated with regions of increased roughness or cleaner surface ice, possibly ice mountains.

Radar cross-section values have been computed by estimating the total power in the Doppler spectra divided by the power that would be received from a smooth, conducting sphere at the same distance and size of Titan. Thus, the cross sections are normalized by the cross-sectional area of Titan. At various times, Titan was observed with either 381-Hz channels or 762-Hz channels, the latter to measure both circular polarizations. A $\cos^n$ power law was fit to the narrow channel data to integrate the total power for these experiments. The

Table 1 Titan radar cross-section measurements at a wavelength of 3.5 cm

Date	Long.	Comments	Distance (AU)	Power (Kw)	Polarization	σ	Error
3/6/89	90	C array	9.3	360	LCP	0.04	0.05
4/6/89	113	C	9.3	360	LCP	0.30	0.05
5/6/89	135	C	9.3	360	LCP	0.13	0.06
all 89	113	C	9.3		LCP	0.15	0.03
22/7/90	65	B	9.0	360	LCP	0.09	0.06
22/7/90	65	B	9.0	360	RCP	0.00	0.08
23/7/90	87	B	9.0	360	LCP	0.19	0.07
23/7/90	87	B	9.0	360	RCP	0.23	0.07
24/7/90	109	B	9.0	355	LCP	0.02	0.08
24/7/90	109	B	9.0	355	RCP	0.00	0.08
all/90	87	B	9.0		LCP	0.12	0.05
21/5/91	54	D	9.5	470	LCP	0.15	0.08
21/5/91	54	D	9.5	470	RCP	0.05	0.09
22/5/91	76	D	9.5	460	LCP	0.39	0.13
22/5/91	76	D	9.5	460	RCP	0.09	0.15
23/5/91	99	D	9.5	460	LCP	0.15	0.06
23/5/91	99	D	9.5	460	RCP	0.01	0.12
21+22+23	76	D	9.5		LCP	0.23	0.06
21+22+23	76	D	9.5		RCP	0.05	0.05
28/5/91	212	D	9.5	460	LCP	0.10	0.06
28/5/91	212	D	9.5	460	RCP	0.00	0.06
all/91		D	9.5		LCP	0.20	0.05
all/91		D	9.5		RCP	0.03	0.05
10/8/92	54	D	8.9	450	LCP	0.15	0.05
10/8/92	54	D	8.9	450	RCP	0.00	0.05
11/8/92	76	D	8.9	450	LCP	0.10	0.05
11/8/92	76	D	8.9	450	RCP	0.13	0.05
all/92	65	D			LCP	0.13	0.04
all/92	65	D			RCP	0.06	0.03
5/8/93	228	C	8.8		LCP	0.07	0.03
6/8/93	250	C	8.8		LCP	0.15	0.06
7/8/93	272	C	8.8		LCP	0.12	0.04
8/8/93	296	C	8.8		LCP	0.08	0.04
9/8/93	320	C	8.8		LCP	0.12	0.04
5+6+7+8+9	273	C	8.8		LCP	0.110	0.0159
12/8/93	50	C	8.7		LCP	0.15	0.03
13/8/93	70	C	8.7		LCP	0.14	0.04
12+13	60	C	8.7		LCP	0.15	0.03
14/8/93	94	C "rain"	8.7		LCP	0.05	0.08
15/8/93	118	C "rain"	8.7		LCP	0.09	0.06
16/8/93	140	C "rain"	8.7		LCP	0.11	0.09

cross-section results for all of the measurements are shown in Table 1. Transmitter logs always indicate that the transmitter was in the RCP mode. The VLA array configuration is indicated as B, C, or D. The A array, being the largest, over-resolves Titan. The B array resolved it down to .85% and the D array was so small that antenna shadowing occurred, requiring extensive data editing. Additionally, in the D array, confusing flux from Saturn affected the data due to the large synthesized beam (7.2 arc sec). The optimum array configuration for Titan is C, which does not resolve the satellite and suffers no antenna shadowing. The tabulated longitudes assume that Titan is in synchronous rotation. The tabulated errors are those in estimating the cross sections and must not be confused with the detection uncertainties, which are much smaller and involve both the visibility amplitudes and phases.

Large variations can be seen in the early experiments, particularly in the D-array data, in part caused by confusion with Saturn's thermal emission. The SS polarization measurements are completely mysterious. Often no signal was detected in RCP, except on 23 July, 1990 and August 11, 1992 when the SS cross sections were larger than the OS cross sections. We believe that the measurements are real and not the result of instrumental errors because there have been no false polarization measurements in our experiences with Mercury, Mars, or Venus, which are essentially identical experiments except for the signal-to-noise ratio. Because the 1993 observations are so extensive and, apparently, the pointing of the transmitter was improved, we concentrate the remaining discussion on these data. The average spectrum for that year (excluding the 3 rainy days at the VLA) is shown in Figure 15. Our best estimate of the mean Titan radar cross section is 0.125 ± 0.02. The Doppler spectral shape is well represented by a $\cos^{1.4} \phi$, where ϕ is the angle of incidence. As proof that these experiments are never perfect, it was necessary to remove a frequency offset from the data, apparently caused by a synthesizer setting error. Titan backscattering is even flatter than a Lambertian surface ($n = 2$), which makes it difficult to understand the daily cross-section variations if the rotation is as slow as the 16 day synchronous period. Furthermore, such flat surfaces (seen on the icy Galilean satellites) suggest either high surface roughness or nearly isotropic scattering from partially transparent media, and they should exhibit nearly random polarization. This was observed on only 2 of 8 days in which polarization measurements were made.

Cross sections plotted as a function of longitudes for synchronous rotation are shown in Figure 16 from all the experiments. The 1993 results are shown as filled points. Except for the 3 days when it rained at the VLA, the results are rather constant with a suggestion of higher reflectivity at the eastern, or approaching elongation (0.15 ± 0.05) than at the western elongation (0.10 ± 0.04). The mean value of the cross section is then 0.125 ± 0.02. Muhleman et al (1992) have speculated that the rotational rate of Titan may be slightly faster

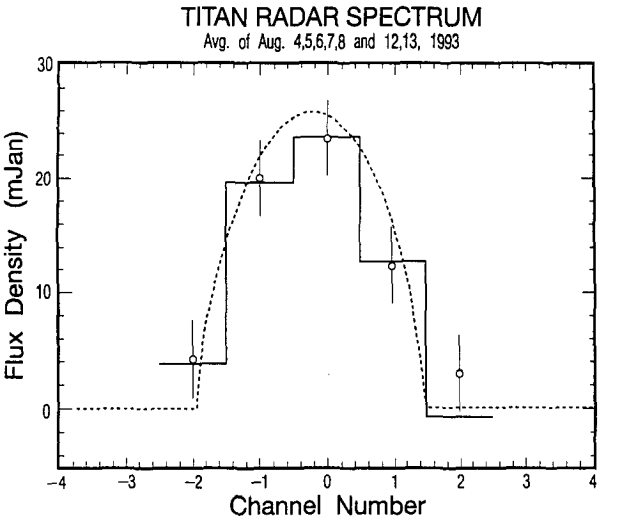

Figure 15 Radar spectrum of Titan at a wavelength of 3.5 cm, averaged over 7 days. The dashed line shows a $\cos^{1.4}\phi$ fit, where ϕ is the angle of incidence. An adjustment was also made for a synthesizer offset of 88 Hz. The data show that the Titan surface scatters the radar signal similarly to that from a Lambert sphere. (From Muhleman et al 1993.)

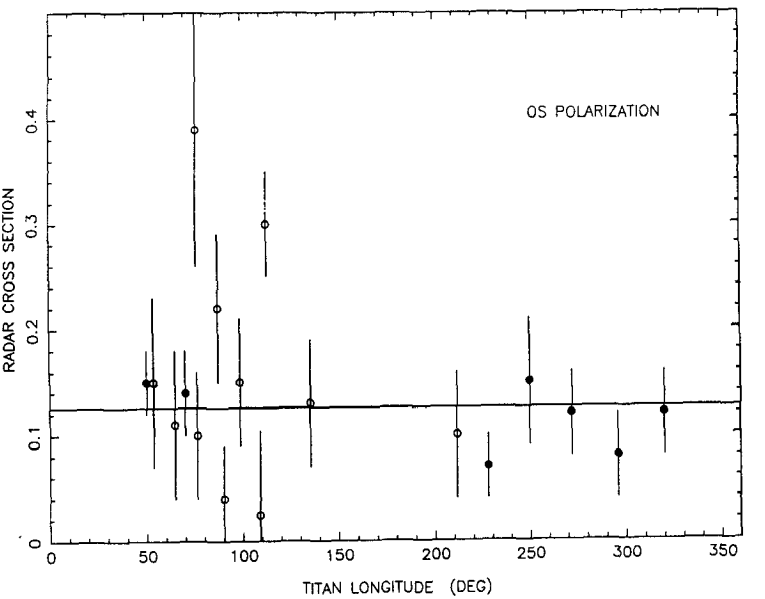

Figure 16 Measured OS radar cross sections of Titan at 3.5-cm wavelength, plotted as a function of the Titan longitudes assuming Titan to be in synchronous rotation. The filled points are from 1993. The mean of these data is 0.125 (0.010). (From Muhleman et al 1993.)

than synchronous, partly because of the rather large orbital eccentricity of 0.029. A period of 15.911 days, compared with a synchronous period of 15.9454 days, would change the longitude system to force the regions of observed high radar cross sections to be aligned. This new system puts the bright region at a longitude that was unobservable in the 1993 experiment! Thus, nothing new was learned about the existence of this bright longitude or the rotation period in the most recent experiment. However, we believe that our measurements provide a weak argument (at best) for other than synchronous rotation.

The measured mean reflectivity of Titan is similar to that of Callisto, except for the ambiguous polarization observations. The 3.5-cm cross section of $0.30 \pm .02$ from Ostro et al (1992) is thought to be consistent with the dirty ice on Callisto's near surface, which depresses its geometrical visual albedo to about 0.22 compared to those of Europa and Ganymede, which are about 0.8 and 0.5, respectively (Johnson & Pilcher 1977). Thus, the collection of Titan radar data to date suggests that the surface of Titan is most like that of Callisto. This correspondence is well illustrated by a figure from Grossman & Muhleman (1995) reproduced here in Figure 17. Measurements for Solar System bodies of radar cross sections are plotted against the microwave emissivity as determined by brightness temperature measurements. The mean value from the 1993 data was used for the cross section of Titan. The solid line indicates

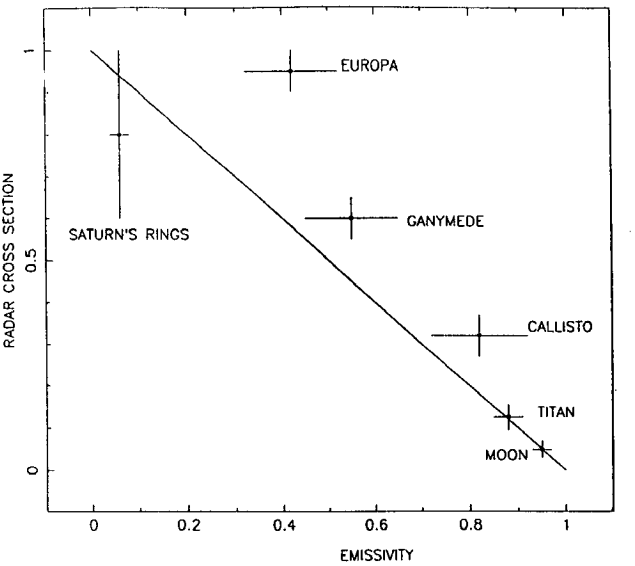

Figure 17 A rough plot of the centimeter wavelength radar cross sections of icy bodies (plus the Moon) against the centimeter emissivity of the objects. The solid line at 45° shows the complimentary relationship between the two variables near which the data should fall. (From Grossman & Muhleman 1995.)

the complementary nature of the two measurements, i.e. that the emissivity and reflectivity should nearly add to unity. This relationship is not expected to strictly hold for our observations because although emissivity is an integrated quantity, measured over all angles, the radar reflectivity is measured just in the backscatter direction. The albedo and radar darkening on Callisto are not understood but may be caused by silicates. A similar effect may exist on Titan but it is reasonable to expect that its surface is partially covered by low reflectivity hydrocarbon solids and liquids in the form of "lakes."

The Titan rotational direction and spin axis orientation will be determined from future VLA radar measurements. Pinning down the exact rotational rate is much more difficult for it requires observing Titan continuously over several orbits and correlating radar features. This may be possible with the upgraded Aercibo radar. Furthermore, the atmospheric window at wavelengths near 1 micron may provide data that will resolve this question in the next few years.

SUMMARY

Radar astronomy techniques continue to improve, making new and more unique experiments possible. The radar facilities at Goldstone can be greatly improved by feasible but expensive increases in transmitter power. That would make the VLA radar configuration far more valuable, allowing snapshots of Mars in a couple of minutes and making use of the highest resolution in the A array practical for Titan and the Galilean satellites. Since the Goldstone radar can scan the entire sky, it is the primary instrument for observing sources such as asteroids and comets in the southern sky or out of the ecliptic. The Arecibo radar is being rebuilt as we write. It will bring radar astronomy into a new era.

Literature Cited

Butler BJ. 1994. *3.5-cm Radar investigation of Mars and Mercury: planetological implications.* PhD thesis. Calif. Inst. Technol., Pasadena (Paper II)

Butler BJ, Muhleman DO, Slade MA. 1993. Mercury: full disk radar images and the detection and stability of ice at the North Pole. *J. Geophys. Res.* 98:15,003–23 (Paper III)

Campbell DB, Arvidson RE, Shepard MK. 1993. Radar polarization properties of volcanic and playa surfaces: applications to terrestrial remote sensing and Venus data interpretation. *J. Geophys. Res.* 98:17,099–113

Campbell DB, Chandler JF, Ostro SJ, Pettengill GH, Shapiro II. 1977. Galilean satellites: 1976 results. *Icarus* 34:254–67

Campbell MJ, Ulrichs RM. 1969. Electrical properties of rocks and their significance for lunar radar observations. *J. Geophys. Res.* 74:5867–81

Carpenter RL, Goldstein RM. 1963. Radar observations of Mercury. *Science* 142:381–82

Carr MH. 1984. Geology of the terrestrial planets. *NASA SP-469*

Carr MH, Clow GD. 1981. Martian channels and valleys: their characteristics. *Icarus* 48:91–117

Davies ME, Dwarnik SE, Gault DE, Strom RG. 1978. Atlas of Mercury. *NASA SP-423*

Evans JV. 1962. Radar echo studies of the Moon. In *Physics and Astronomy of the Moon,* ed. Z. Kopal, chap. 12. London: Academic

Evans JV, Hagfors T, eds. 1968. *Radar Astronomy.* New York: McGraw-Hill
Goldstein RM, Gilmore WF. 1963. Radar observations of Mars. *Science* 141:1171–72
Goldstein RM, Green RR. 1980. Ganymede: radar surface characteristics. *Science* 207: 179–80
Goldstein RM, Morris GA. 1975. Ganymede: Observations by radar. *Science* 188:1211–12
Green PE. 1968. Radar measurements of target scattering properties. See Evans & Hagfors 1968, chap. 1
Griffith CA. 1993. Evidence for surface heterogenity on Titan. *Nature* 364:511–14
Griffith CA, Owen TC, Wagener R. 1991. Titan's surface and troposphere investigated with groundbased, near-infrared observations. *Icarus* 93:362–78
Grossman AW, Muhleman DO. 1995. The microwave light-curve of Titan.
Hagfors T, Kofman W. 1991. Mapping of overspread targets in radar astronomy. *Radio Sci.* 26:403–16
Hapke B. 1990. Coherent backscatter characteristics of the outer planet satellites. *Icarus* 88:407–17
Hapke B, Blewitt D. 1991. Coherent backscatter model for the unusual radar reflecivity of icy satellites. *Nature* 352:46–47
Harmon JK, Ostro SJ. 1985. Mars: dual-polarization radar observations with extended coverage. *Icarus* 62:110–28
Harmon JK, Slade MA. 1992. Radar mapping of Mercury: full-disk delay-Doppler mapping. *Science* 258:640–43
Harmon JK, Slade MA, Hudson RS. 1992b. Mars radar scattering: Arecibo/Goldstone results at 12.6-cm and 3.5-cm wavelengths. *Icarus* 98:240–53
Harmon JK, Slade MA, Velez RA, Crespo A, Dryer MJ, Johnson JM. 1994. Radar mapping of Mercury's anomalies. *Nature* 369: 213–15
Harmon JK, Sulzer MP, Perillat PJ, Chandler JF. 1992a. Mars radar mapping: strong backscatter from the Elysium basin and outflow channel. *Icarus* 95:153–56
Hubbard WB. et al. 1993. The occulatation of 28 Sgr by Titan. *Astron. Astrophys.* 269:542–63
Hughes HG, App FM, McGetchen T. 1977. Global seismic effects at basin-forming forming impacts. *Phys. Earth Planet. Inter.* 15:251–63
Hunten DM, Tomasko MG, Flaser FM, Samuelson RE, Strobel DE, Stevenson DJ. 1984. In *Saturn,* ed. T. Gehrels, MS Matthews, pp. 671–759. Tucson: Univ. Ariz. Press
Johnson JV, Pilcher CB. 1977. Satellite spectrophotometry and surface compositions. In *Planetary Satellites,* ed. J Burns, pp. 232–68. Tucson: Univ. Ariz. Press
Kieffer HH, Martin TZ, Peterfreund AR, Jakosky BM, Miner ED, Palluconi FD. 1977. Thermal and albedo mapping of Mars during the Viking primary mission. *J. Geophys. Res.* 82:4249
Lemmon MT, Karkoschka E, Tomoasko M. 1993. Titan's rotation: surface features observed. *Icarus* 103:329–32
Lindal GF, Wood GE, Hotz HB, Sweetnam DN, Eshleman VR, Tyler GL. 1983. The atmosphere of Titan: an analysis of the Voyager 1 radio occultation measurements. *Icarus* 53:348–63
Lunine JI. 1994. Does Titan have oceans? *Am. Sci.* 82:134–43
Lunine JI, Stevenson DJ, Yung YL. 1983. Ethane ocean on Titan. *Science* 222:1229–30
Muhleman DO, Berge GL. 1991. Observations of Mars, Uranus, Neptune, Io, Europa, Ganymede, and Callisto at a wavelength of 2.66 mm. *Icarus* 92:263–71
Muhleman DO, Butler BJ, Grossman AW, Slade MA. 1991. Radar images of Mars. *Science* 253:1508–13 (Paper I)
Muhleman DO, Goldstein RM, Carpenter R. 1965. A review of radar astronomy. Part 1. *IEEE Spectrum* 2:44–55; Part 2. 2:78–89
Muhleman DO, Grossman AW, Slade MA, Butler BJ. 1990. Radar reflectivity of Titan. *Science* 248:975–80
Muhleman DO, Grossman AW, Slade MA, Butler BJ. 1992. The surface of Titan and Titan's rotation: what is radar telling us? *Bull. Am. Astron. Soc.* 24:954
Muhleman DO, Grossman AW, Slade MA, Butler BJ. 1993. Titan's radar reflectivity and rotation. *Bull. Am. Astron. Soc.* 25:1099
Murray BM, Belton MJS, Danielson GE, Davies ME, Gault DE, et al. 1974. Mercury's surface: preliminary description and interpretation from Mariner 10 pictures. *Science* 185:169–79
Ostro SJ. 1982. Radar properties of Europa, Ganymede and Callisto. In *Satellites of Jupiter,* ed. D. Morrison, pp. 213–36. Tucson: Univ. Ariz. Press
Ostro SJ. 1993. Planetary radar astronomy. *Rev. Mod. Phys.* 65:1235–79
Ostro SJ, Campbell DB, Simpson RA, Hudson RS, Chandler JF, et al. 1992. Eoropa, Ganymede, and Callisto: new results from Arecibo and Goldstone. *J. Geophys. Res.* 97:18,227–44
Owen TC, Roush TL, Cruikshank DP, Elliot JL, Young LA. 1993. Surface ices and the atmospheric composition of Pluto. *Science* 261:745
Paige DA, Wood SE, Vasavada AR. 1992. The thermal stability of water ice at the poles of Mercury. *Science* 258:643–46
Palluconi FD, Kieffer HH. 1981. Thermal inertia mapping of Mars from 60°S to 60 °N *Icarus* 45:415–26
Peale SJ. 1988. The rotational dynamics of Mercury and the state of its core. In *Mercury,* ed.

F Vilas, MS Matthews, pp. 460–93. Tucson: Univ. Ariz. Press
Pettengill GH. 1960. Unpublished lecture notes, MIT
Pettengill GH. 1965. A review of radar studies of planetary surfaces. *Radio Sci. J. Res. Natl. Bur. Stand.* 69D:1617–23
Pettengill GH, Henry JC. 1962. Radar measurements of the lunar surface. In *The Moon, IAU Symp. 14,* ed. Z. Kopal, p. 519. London: Academic
Plescia JB. 1990. Recent flood lavas in the Elysium region of Mars. *Icarus* 88:465–90
Schultz PH, Lutz AB. 1988. Polar wandering of Mars. *Icarus* 73:91–141
Scott DH, Tanaka KL. 1986. Geological map of the western equatorial region of Mars. *USGS map I-1802-A*
Scott DH, Tanaka KL. 1982. Ignimbrites of Amazonis Planita region of Mars. *J. Geophys. Res.* 87:1179–90
Simpson RA, Harmon JK, Zisk SJ, Thompson TW, Muhleman DO. 1992. Radar determination of Mars surface properties. In *Mars,* ed. H. Keifer, B. Jakosky, pp. 652–85. Tucson: Univ. Ariz. Press
Slade MA, Butler BJ, Muhleman DO. 1992. Mercury radar imaging: evidence for polar ice. *Science* 258:635–40
Stratton JA. 1941. *Electromagnetic Theory.* New York/ London: McGraw-Hill
Tanaka JK, Scott DH. 1980. Channeling and flooding on Mars. *Proc. Third Colloq. Planetary Water,* pp. 76–80 (Abstr.)
Thompson AR, Moran JM, Swenson Jr. 1986. Interferometry and synthesis. In *Radio Astronomy.* Malabar, FL: Krieger
Thompson TW, O'Brien TC, Jurgens RF, Slade MA, Moore HJ. 1992. Mars quasi-specular echoes: preliminary results at 3.5-cm wavelength. *Proc. Lunar Sci. Conf. XXIII,* pp. 1431–32. Houston: Lunar Planet. Inst.
Tryka KA, Muhleman DO. 1992. Reflection and emission properties on Venus: Alha Regio. *J. Geophys. Res.* 97:13,379–94
Tyner RL, Carroll RD. 1983. *A Catalog of Selected Viking Orbiter Images. NASA Ref. Pub. 1093*

Annual Review of Earth and Planetary Sciences
Volume 23, 1995

CONTENTS